

# Topology from the Simulated Sloan Digital Sky Survey

Wesley N. Colley<sup>1</sup>, J. Richard Gott, III<sup>2</sup>, David H. Weinberg<sup>3</sup>, Changbom Park<sup>4</sup> and Andreas A. Berlind<sup>3</sup>

## ABSTRACT

We measure the topology (genus curve) of the galaxy distribution in a very large cosmological simulation designed to resemble closely results from the upcoming Sloan Digital Sky Survey (SDSS). The mock survey is based on a large N-body simulation that uses 54,872,000 particles in a periodic cube  $600h^{-1}\text{Mpc}$  on a side. The adopted inflationary cold dark matter (CDM) model has parameters  $\Omega_{\text{CDM}} = 0.4$ ,  $\Omega_{\Lambda} = 0.6$ ,  $h = 0.6$ ,  $b = 1.3$ . We “observe” this simulation to produce a simulated redshift catalog of  $\sim 10^6$  galaxies over  $\pi$  steradians, mimicking the anticipated spectroscopic selection procedures of the SDSS in some detail. Sky maps, redshift slices, and 3-D contour maps of the mock survey reveal a rich and complex structure, including networks of voids and superclusters that resemble the patterns seen in the CfA redshift survey and the Las Campanas Redshift Survey (LCRS). The 3-D genus curve can be measured from the simulated catalog with superb precision; this curve not only has the general shape predicted for Gaussian, random phase initial conditions, but the error bars are small enough to demonstrate with high significance the subtle departures from this shape caused by non-linear gravitational evolution on a  $10h^{-1}\text{Mpc}$  smoothing scale (where  $\sigma_{\text{gal}} = 0.4$ ). These distortions have the form predicted by Matsubara’s (1994) perturbative analysis, but they are smaller in amplitude. We also measure the 3-D genus curve of the radial peculiar velocity field measured by applying distance-indicator relations (with realistic errors) to the mock catalog. The genus curve is consistent with the Gaussian random phase prediction, though it is of relatively low precision because of the large smoothing length required to overcome noise in the measured velocity field. Finally, we measure the 2-D topology in redshift slices, similar to those which will become available early in the course of the SDSS and to those already observed in the LCRS. The genus curves of these slices are consistent with the observed genus curves of the LCRS, suggesting that our inflationary CDM model with  $\Omega_{\text{CDM}} \sim 0.4$  is a good choice. Our mock redshift catalog is publicly available for the use of other researchers.

---

<sup>1</sup>Harvard-Smithsonian Center for Astrophysics, 60 Garden Street, Cambridge MA 02138, wcolley@cfa.harvard.edu

<sup>2</sup>Princeton University Department of Astrophysical Sciences, Princeton, NJ 08544, jrg@astro.princeton.edu

<sup>3</sup>Department of Astronomy, The Ohio State University, 174 W 18th Ave., Columbus, OH 43210-1106, dhw,aberlind@astronomy.ohio-state.edu

<sup>4</sup>Department of Astronomy, Seoul National University, Seoul 151, Korea, cbp@astro.snu.ac.kr

## 1. Introduction

The nature of large-scale structure in the universe is one of the pre-eminent questions of modern astronomy. Gravitational growth of structure from quantum fluctuations during inflation has become the leading candidate for production of this structure. The topology of large-scale structure as quantified by the “genus curve” (Gott, Melott, & Dickinson 1986, hereafter GMD; Hamilton, Gott, & Weinberg 1986; Gott, Weinberg, & Melott 1987, hereafter GWM) tests one of the most robust predictions of inflation, namely that the quantum fluctuations produce a Gaussian random phase field of density perturbations, the seeds of the structures seen today. To date, all topological studies of galaxy redshift surveys (in 3-D and 2-D) and cosmic microwave background (CMB) anisotropies (in 2-D) have been consistent with Gaussian random phase initial conditions (Gott et al. 1989; Moore et al. 1992; Park, Gott, & da Costa 1992; Gott, Rhoads, & Postman 1994; Vogeley et al. 1994; Colley, Gott, & Park 1996; Kogut et al. 1996; Colley 1997; Protogeros & Weinberg 1997; Canavezes et al. 1998; Springel et al. 1998).

The genus test becomes only more powerful as cosmological surveys become larger. While several prodigious observational efforts have been made to survey the large-scale structure traced by optical galaxies (Geller & Huchra 1989; Shectman et al. 1996) and by IRAS galaxies (Canavezes et al. 1998 and references therein), the 2-degree Field (2dF) redshift survey (see Colless 1998) and the Sloan Digital Sky Survey (SDSS)<sup>5</sup> will dwarf all currently existing redshift surveys in data volume. The SDSS will obtain approximately one million galaxy redshifts (compared to  $\sim 250,000$  anticipated for 2dF), and the resulting high-precision measurement of the three-dimensional topology will therefore provide a far more powerful test of the random phase hypothesis than is possible today. In order to prepare for topological analysis and other statistical studies of this enormous sample, we have created a simulation of the SDSS using a very large N-body simulation ( $N = 54,827,000$  particles). In this paper we show that the three-dimensional genus curve can be measured with unprecedented precision from the SDSS, as anticipated. We also show that it should be possible to measure the topology of the smoothed radial velocity field inferred from the SDSS images and spectra via distance-indicator relations.

Early on in the SDSS, two-dimensional redshift slices, comparable to the deepest existing wide-angle redshift surveys, such as the Las Campanas Redshift Survey (LCRS, Shectman et al. 1996), will allow studies of the two-dimensional genus curve. Colley (1997) computed the two-dimensional topology of large-scale structure observed in the LCRS. We have therefore generated slices from our Simulated SDSS (SSDSS), intended to match closely those of the LCRS. We use particular statistical care to compare the topology of our simulation slices to that of the observed slices from the LCRS. Redshift slices (of constant angle in the sky) are complementary

---

<sup>5</sup>Detailed information about the SDSS can be found in the collaboration’s NASA proposal, available at <http://www.astro.princeton.edu/BBOOK/>, which we refer to henceforth as Knapp et al. (1997). Review articles describing the survey in more general terms include Gunn & Knapp (1993), Gunn & Weinberg (1995), and Margon (1999).

to maps of the CMB, which mainly probe a shell at constant radius ( $z \sim 1000$ ). The topology of CMB fluctuations as observed by COBE (Smoot et al. 1994) has been computed by Colley et al. (1996) and Kogut et al. (1996). A similar 2-D topological approach has been applied to projected galaxy and cluster catalogs by Gott, Mao, Park & Lahav (1992), Plionis, Valdarnini, & Coles (1992), Coles et al. (1993), and Davies & Coles (1993).

## 2. The Cosmological Simulation

The SDSS will measure the redshifts of approximately  $10^6$  galaxies in  $\pi$  steradians of the northern sky. This observational sample should provide an unprecedented opportunity to measure quantitatively the 3-D and 2-D topology of large-scale structure in the universe.

Since, at its best, theory should predict observations *before* they are taken, we felt it important to simulate *ahead* of time the results to be obtained by the SDSS. One purpose of this is cosmological model testing, of course, but no less importantly we hope to show in a general way what features may be expected from a gravitational instability model. Perhaps most important of all, we hope to illustrate just how powerful the SDSS will be, i.e., just how accurately it will allow us to measure statistical quantities of interest, such as the genus curve. To this end, we have run a very large N-body simulation intended to mimick results from the SDSS.

In 1992 the results from COBE (Smoot et al. 1992; Wright et al. 1992) provided great support for the gravitational instability picture by finally showing the long sought fluctuations in the microwave background predicted by this theory. The fluctuations found by COBE were consistent with a Harrison (1970)-Peebles & Yu (1970)-Zeldovich (1972) spectrum of fluctuations with a primordial index  $n = 1$ , Gaussian random phases (e.g. Colley et al. 1996; Kogut et al. 1996), and a standard, unbiased ( $b \approx 1$ ),  $\Omega = 1$ ,  $h = 0.5$  (where  $h \equiv H_0/[100 \text{ km/s/Mpc}]$ ), inflationary cold dark matter (CDM) universe. It is noteworthy that the fluctuations seen by COBE are on scales larger than the horizon size at recombination, just the sort of fluctuations one would expect from random quantum fluctuations in a standard inflationary model (Guth 1981).

While CDM inflationary models allow low amplitude microwave background fluctuations like those observed by COBE, they simultaneously produce structure which matches that observed at redshifts  $z \lesssim 5$ , because the smoothly distributed baryons can fall into pre-existing CDM potential wells *after* recombination and because the hierarchical form of the inflationary CDM power spectrum (Bardeen, Steinhardt, & Turner 1983) allows early formation of quasars and galaxies. Furthermore, adiabatic Gaussian fluctuations with this initial  $n = 1$  power spectrum have proven amazingly successful at explaining the qualitative features of observed galaxy clustering, including the characteristic pattern of great walls and giant voids seen in the Geller & Huchra (1989) slices (White et al. 1987; Park 1990; Weinberg & Gunn 1990a) and lattice-like sequences of great walls in deep pencil beam surveys (Broadhurst et al. 1990; Park & Gott 1991a). Other successes of CDM include this very wide variety of remarkable properties in common with observation: deep sky

maps show clusters, but are bland compared to  $6^\circ$  slices which show large voids;  $20^\circ$  wide slices show great walls; velocity fields show great attractors; the 3-D topology is spongelike; deep pencil beams show surprisingly regular lattices of great walls out to  $z = 0.5$ ; deep slices to  $z = 0.2$  show a more uniform appearance than shallow slices to  $z = 0.05$ ; the cluster-cluster covariance function is a higher amplitude version of the galaxy-galaxy covariance function (Bahcall & Soneira 1983; Klypin & Kopylov 1983); and the three-point correlation functions of clusters and galaxies show the same triangular form (Gott, Gao, & Park 1991). Even if one were given complete freedom to construct an arbitrary, multi-parameter, geometrical model of large-scale structure, it is hard to see how one could come up with something that would reproduce all of these qualitative and quantitative successes of the physically motivated, dynamical model of gravitational structure formation from Gaussian initial conditions with an inflationary CDM power spectrum.

Within the inflationary CDM paradigm, there are many reasons for selecting a model with  $\Omega \approx 0.4$ . In models with scale-invariant inflationary fluctuations ( $n = 1$ ), CDM-dominated matter content ( $\Omega_{\text{HDM}} \ll \Omega_{\text{CDM}}$ ;  $\Omega_B \ll \Omega_{\text{CDM}}$ ), and a standard relativistic background (CMB photons plus the usual light neutrino species), a low value of  $\Omega h$  is required to explain the observed shape of the galaxy power spectrum (see Peacock & Dodds 1994 and numerous references therein) and the observed amplitude of the 3-D galaxy genus curve at large smoothing scales (see Moore et al. 1992; Vogeley et al. 1994; Canavese et al. 1998). With the same restrictions, a value of  $\Omega \sim 0.25 - 0.5$  is required to match simultaneously the COBE fluctuation amplitude and the mass function of galaxy clusters for  $t_0 \approx 13$  Gyr (Cole et al. 1997 and references therein). Direct evidence for  $\Omega \approx 0.4$  includes the combination of the cluster baryon fraction with big bang nucleosynthesis constraints (Evrard 1997) and the combination of the  $z = 2.5$  mass power spectrum inferred from the Lyman-alpha forest with the  $z = 0$  cluster mass function (Weinberg et al. 1998). This value of  $\Omega$  is consistent with some analyses of galaxy cluster evolution (e.g., Bahcall, Fan, & Cen 1997; Eke, Cole, & Frenk 1998) but not with others (e.g., Blanchard & Bartlett 1998; Reichart et al. 1998; Viana & Liddle 1998). With a modest bias of the galaxy population in clusters it is consistent with observed cluster mass-to-light ratios (Carlberg et al. 1996, 1997).

Once one adopts low  $\Omega$ , the inclusion of a cosmological constant  $\Omega_\Lambda = 1 - \Omega$  is theoretically attractive (Ratra & Peebles 1998; Peebles & Ratra 1998) because it maintains the flat spatial geometry that seems the most natural prediction of inflation, requiring no fine-tuning of the number of inflationary  $e$ -folds (though fine-tuning is still required to explain the present-day value of  $\Omega_\Lambda$ ). Such a model could arise naturally within Linde's (1990) chaotic inflation scenario. Flat geometry also appears to be favored by some preliminary measurements of the angular location of the first Doppler peak in the CMB multipole spectrum (see, e.g., discussions by Lineweaver [1998] and Tegmark [1998]). A cosmological constant makes it easy to reconcile values of  $h \sim 0.6 - 0.8$  with the inferred ages of the oldest globular clusters. A value of  $\Omega_\Lambda = 0.6$  is low enough that gravitational lensing cross-sections are not an embarrassment (Fukugita et al. 1992), and indeed Chiba & Yoshii (1999) argue that gravitational lensing statistics favor a value of  $\Omega_\Lambda$  in this range. The recent inference of an accelerating cosmic expansion from observations

of Type Ia supernovae (Riess et al. 1998; Perlmutter et al. 1999) provides additional and more direct evidence for a cosmological constant or some similar negative-pressure component of the universe. These and other arguments in favor of a low-density, flat universe have been summarized by a number of authors, including a recent analysis by Roos & Harun-or-Rashid (1999), who show that the combination of a variety of independent constraints favors  $\Omega_\Lambda = 0.70 \pm 0.14$  and  $\Omega_M + \Omega_\Lambda = 0.99 \pm 0.16$  ( $1\sigma$  error bars) even *without* the supernova data.

An alternative to the  $\Lambda$ CDM model is an open model with  $\Omega_{\text{CDM}} < 1$  and  $k = -1$ . An open universe can be produced in single-bubble inflationary models (cf. Gott 1982; Gott & Statler 1984; Gott 1986; Ratra & Peebles 1994, 1995; Bucher et al. 1995a,b; Yamamoto et al. 1995; Linde 1995; Linde & Mezhlumian 1995; Hawking & Turok 1998). An  $\Omega = 0.4$ ,  $\Omega_\Lambda = 0.6$ ,  $b = 1.3$  model is quite similar, in terms of galaxy clustering, to an  $\Omega = 0.4$ ,  $\Omega_\Lambda = 0$ ,  $b = 1.3$  model, so our simulation can serve reasonably well as a stand-in for either.

Ratra et al. (private communication) find the following 4-year-COBE normalized values with  $2\sigma$  limits, all assuming  $\Omega_B h^2 = 0.0125$ :

$$\begin{aligned}
 & \Omega = 1, \Omega_\Lambda = 0, h = 0.54, t_0 = 12 \text{ Gyr}, \\
 & \Omega h = 0.54, \sigma_8 = 1.1\text{--}1.5, 0.7 < b < 0.9; \\
 & \Omega = 0.4, \Omega_\Lambda = 0.6, h = 0.6, t_0 = 14.5 \text{ Gyr}, \quad (1) \\
 & \Omega h = 0.24, \sigma_8 = 0.82\text{--}1.2, 0.8 < b < 1.22; \\
 & \Omega = 0.4, \Omega_\Lambda = 0, h = 0.63, t_0 = 12 \text{ Gyr}, \\
 & \Omega h = 0.252, \sigma_8 = 0.51\text{--}0.74, 1.35 < b < 1.96.
 \end{aligned}$$

Thus our simulation's bias parameter  $b = 1.3$  (our simulation was done before the COBE 4-year normalization was available) is just above the  $0.8 < b < 1.22$  COBE 4-year normalization, so it has only marginally high bias. Its bias is slightly below the COBE 4-year normalization for an  $\Omega = 0.4$ ,  $\Omega_\Lambda = 0$  model ( $1.35 < b < 1.96$ ). This modest level of bias is consistent with the predictions of hydrodynamic cosmological simulations (e.g., Cen & Ostriker 1992; Katz, Hernquist, & Weinberg 1992) and semi-analytic models of galaxy formation (e.g., Kauffmann, Nusser, & Steinmetz 1997).

We thus adopt a CDM inflationary model with cosmological parameter values  $\Omega = 0.4$ ,  $\Omega_\Lambda = 0.6$ ,  $k = 0$ ,  $h = 0.6$ ,  $t_0 = 14.5$  Gyr, and r.m.s. fractional mass fluctuation  $\sigma_8 = 1/b = 0.77$  in spheres of radius  $8h^{-1}\text{Mpc}$ . These values arguably provide the best fit to all current observational constraints. (Ostriker & Steinhardt [1995] independently picked as their favored model one with similar parameters; Turner [1998] also independently arrived at these as a promising set of parameters, roughly consistent with recent Type Ia supernovae data from Riess et al. [1998] and Perlmutter et al. [1999], which favor  $\Omega \sim 0.2\text{--}0.3$ .)

Our N-body simulation uses  $N = 380^3 = 54,872,000$  particles (the simulation was run in 1993; some results from it were published in Vogeley et al. [1994], prior to the appearance

of this paper). The simulation uses a staggered-grid, particle-mesh code (Park 1990) with a  $600^3$  density-potential mesh and a simulation volume of  $(600h^{-1}\text{Mpc})^3$ . Thus our gravitational force resolution is  $\sim 1h^{-1}\text{Mpc}$ . A biased subset of 8,292,455 particles are chosen to represent galaxies, chosen as peaks that lie above a threshold  $\delta/\delta_{rms} = 0.8$  when the CDM density field is smoothed over  $0.71h^{-1}\text{Mpc}$ . The peak particles are identified using the Bardeen et al. (1986) peak-background split approximation, as discussed by Park (1991). This combination of smoothing scale and peak threshold yields a bias factor  $b = 1.3$  between the r.m.s. fluctuations of galaxy particles and dark matter on large scales.

### 3. The Mock Redshift Catalog

We have attempted to model the anticipated selection properties of the SDSS redshift survey in some detail, in part because our simulated redshift survey is being used for a number of internal tests of the survey data analysis software and observing strategy. The present observational plan is to select galaxies in the main redshift sample based on their Petrosian (1976) magnitudes and half-light surface brightnesses in the  $r'$  band (see Fukugita et al. [1996] and Gunn et al. [1998] for discussions of the SDSS photometric system). Definitions of our Petrosian magnitude system and motivation for its use are given by Gunn & Weinberg (1995). In the notation of that paper we adopt parameters  $f_1 = 1/8$  and  $f_2 = 2$  for our mock redshift catalog, which means that we define magnitudes within a circular aperture of radius  $2R_P$ , where the Petrosian radius  $R_P$  is the radius at which the local surface brightness falls to 1/8 of the mean interior surface brightness. As a result of more recent tests, the SDSS is likely to adopt somewhat different values of  $f_1$  and  $f_2$ , but we do not expect these changes to substantially alter the survey selection function, since the magnitude limit will be adjusted to ensure the desired number of galaxy targets over the  $\pi$ -steradian survey area.

In order to compute the quantities used for target selection, we first assign two fundamental parameters to each of the 8,292,455 galaxy particles: a  $B_T$  luminosity and a Hubble type. The  $B_T$  luminosities are randomly drawn from a Schechter (1976) luminosity function with parameters  $M_* = -19.68 + 5 \log h$ ,  $\alpha = -1.07$ , truncated below  $0.064L_*$  (about 3 magnitudes below  $M_*$ ) so that the space density of galaxies above the cutoff matches the space density  $\bar{n} = 0.038h^3\text{Mpc}^{-3}$  of galaxies in the N-body simulation. Hubble types E–Sc are assigned randomly, with probabilities modified according to local galaxy density in accord with the Postman & Geller (1984) morphology-density relation (see Narayanan, Berlind, & Weinberg [1998] for details). Bulge-to-disk ratios are assigned as a function of Hubble type based on Kent (1985), and bulge axis ratios are drawn from the distribution inferred by Ryden (1992). Spheroid half-light radii are assigned using Maoz & Rix's (1992) parametrization of the fundamental plane (Djorgovski & Davis 1985; Dressler et al. 1987) for ellipticals, modified according to Fig. 5(b) of Kent (1985) for spiral bulges. Disk half-light radii are assigned using Freeman's (1970) value for the typical central surface brightness. We add Gaussian scatter with r.m.s. of 0.15 in  $\log_{10} D$  to

the diameters  $D$  in order to ensure a population of high and low surface brightness galaxies; this scatter may be unrealistically large, at least for the bulge components. We compute K-corrected magnitudes in the SDSS filters using the spectral-energy distributions of Coleman, Wu, & Weedman (1980). Finally, we compute Petrosian magnitudes and half-light surface brightnesses assuming a de Vaucouleurs (1948) profile for the bulge components and an inclined exponential profile for the disk components.

We adopt a half-light surface brightness threshold  $\mu_{1/2} = 22$  mag arcsec $^{-2}$  and a Petrosian magnitude limit  $r' = 17.9$  (on the AB magnitude system, Oke & Gunn [1983]), yielding 872,377 galaxies in the mock redshift catalog. The SDSS currently plans to target  $\sim 10^5$  luminous red ellipticals in addition to the main galaxy sample, using photometric redshifts to obtain a sparse, nearly volume-limited sample extending to  $z \sim 0.4$ . We attempt to model only the  $\sim 9 \times 10^5$  main galaxy sample here because of the size of our simulation cube.

Once we have decided which galaxies are bright enough to be included in the mock catalog (with origin at a corner of the periodic simulation cube), we need to set the survey sky coverage. The north Galactic cap portion of the SDSS will target a roughly elliptical region,  $130^\circ$  by  $110^\circ$ . One may construct this region by choosing a polar coordinate system  $(\theta, \phi)$  centered on the center of the ellipse. The two foci A and B of the ellipse are along the major axis, each at a distance  $\theta_F = 42.54^\circ = \cos^{-1}[\cos(130^\circ/2)/\cos(110^\circ/2)]$ . Let  $(\theta_g, \phi_g)$  be the polar coordinates of a galaxy in the sky. Its angular distances in the sky from foci A and B respectively are:

$$\begin{aligned}\theta_{gA} &= \cos^{-1}[\sin \theta_F \sin \theta_g \cos \phi_g + \cos \theta_g \cos \theta_F] \\ \theta_{gB} &= \cos^{-1}[-\sin \theta_F \sin \theta_g \cos \phi_g + \cos \theta_g \cos \theta_F].\end{aligned}\quad (2)$$

The galaxy is included in the elliptical survey region if

$$\theta_{gA} + \theta_{gB} \leq 130^\circ \quad (3)$$

Fig. 1 shows a sky map of the  $\sim 900,000$  galaxies in the survey region. This figure bears a remarkable qualitative resemblance to the map of the real sky derived from the Shane-Wirtanen (1967) counts (reproduced on page 41 of Peebles [1993]), which reach to similar depth (without redshifts, of course).

Fig. 2 shows how a  $6^\circ \times 130^\circ$  slice along the major axis of the survey looks when the observed galaxies are plotted in redshift space. Galaxy redshifts are converted into comoving distances using the redshift-comoving distance relation of the  $\Omega_\Lambda = 0.6$ ,  $\Omega = 0.4$  cosmological model. (A simple cubic approximation to this relation,  $r_c = 3000z - 940z^2 + 130z^3 h^{-1}\text{Mpc}$ , has a maximum error of  $0.46h^{-1}\text{Mpc}$  out to  $z = 0.4$ .) The observer is located at the vertex of the fan, which extends to a redshift corresponding to a comoving distance of  $500h^{-1}\text{Mpc}$ . Because we have a lower luminosity limit for galaxies (3 magnitudes below  $M_*$  in  $B$ ), this magnitude-limited sample is incomplete at distances below  $\sim 130h^{-1}\text{Mpc}$ ; the combination of this limit with the decreasing physical width of the slice causes the apparent deficit of galaxies near the vertex of the fan. In the region from  $130h^{-1}\text{Mpc}$  to  $400h^{-1}\text{Mpc}$  where the density of galaxies is highest and the clustering is most

easily seen, we find a wealth of structure. The many small “fingers of god” pointing toward the observer show the locations of clusters; each “finger” corresponds to a roughly spherical cluster, which is stretched in redshift space by the peculiar velocities of its member galaxies. Many voids can be seen with typical sizes of  $30h^{-1}\text{Mpc}$  to  $50h^{-1}\text{Mpc}$ , quite similar to those observed in the de Lapparent, Geller & Huchra (1986)  $6^\circ$  slice, which goes out to  $150h^{-1}\text{Mpc}$ . This pattern of voids is quite typical of CDM models (cf. Park 1990). Many small and “great” walls (Geller & Huchra 1989) are visible, frequently up to  $150h^{-1}\text{Mpc}$  in length, corresponding to the “pancake” structures that Zel’dovich (1970) argued would be a natural consequence of gravitational clustering from Gaussian initial conditions (see also Shandarin & Zel’dovich 1989). There is even a “great wall complex” extending for  $\sim 400h^{-1}\text{Mpc}$  across the slice, at distances  $\sim 150 - 300h^{-1}\text{Mpc}$  from the observer. Such features are also seen in  $\Omega = 1$ ,  $h = 0.5$ ,  $b = 2$  CDM models (Park 1990). The visual difference between this model with  $\Omega h = 0.24$  and a standard  $\Omega h = 0.5$  CDM model is in the low amplitude, rolling hills and valleys in the distribution. The extra modulation of the basic network of voids and walls reflects the extra power on large scales present in an  $\Omega h = 0.24$  CDM model. Nonetheless, we can see that the structure in the slice is approaching a qualitatively “fair sample” of this simulated universe: this fan has a much more uniform appearance than the de Lapparent et al. (1986)  $6^\circ$  slice, which only went out to  $150h^{-1}\text{Mpc}$ . Any theory based on Friedmann cosmological models must approach uniformity on large scales. In the  $\Omega h = 0.24$  CDM model, the power spectrum  $P(k)$  peaks at wavelength  $\lambda \sim 260h^{-1}\text{Mpc}$ , and it drops at larger scales, approaching  $P(k) \propto k$  at very long wavelengths.

In addition to large voids  $30-50h^{-1}\text{Mpc}$  across, there are some void complexes approximately  $100h^{-1}\text{Mpc}$  across (like the one at 1 o’clock at  $250h^{-1}\text{Mpc}$  distance), where we have several low density voids next to each other separated by only relatively weak walls. Weinberg & Gunn (1990b) show time sequences of the formation of such void complexes in models with  $k^{-1}$  power spectra. Galaxies drain off the walls between voids, and the walls eventually become so tenuous that they are barely noticeable. As pointed out by Park et al. (1992), such a case of a tenuous wall inside a large void is seen in the famous de Lapparent et al. (1986) slice. As a CDM model evolves in time, voids grow by galaxies flowing off of minor caustics onto major caustics. This is also the mechanism for the enhancement of great walls.

Overall this slice, which goes to a depth of  $500h^{-1}\text{Mpc}$ , looks remarkably like the sandwich of three  $1.5^\circ$  wide slices (with two  $1.5^\circ$  wide gaps) from the LCRS (Shectman et al. 1996). Since our simulation was run before completion of the LCRS, we were delighted to see how the LCRS qualitatively confirmed many of the features of our simulation slice. It shows the same wall and void structure, the same rolling density at large scales, the same void and wall complexes, and the same overall approach to uniformity on very large scales. The LCRS shows a power spectrum consistent with CDM and  $0.2 < \Omega h < 0.3$  (Lin et al. 1996) and a 2-D topology consistent with random phase initial conditions (Colley 1997), as assumed in our simulation.

#### 4. Measuring the 3-D Topology of Large-Scale Structure

Figs. 3(*a*) and 3(*b*) show contours of constant density in a subset of the three-dimensional simulation out to  $500h^{-1}\text{Mpc}$ . We have created a volume-limited sample for these figures by throwing out those galaxies that would not be visible at  $500h^{-1}\text{Mpc}$ . After smoothing with a Gaussian filter of radius  $R_s = 10h^{-1}\text{Mpc}$ , we have selected contour surfaces at the median density contour [3(*a*)], and at the 93rd-percentile density contour [3(*b*)] (such that the 7% of the volume with highest density is contained within this contour). The median density contour surface is sponge-like, as expected from Gaussian random phase initial conditions (GMD), while Fig. 3(*b*) shows isolated clusters at the 93rd-percentile density, as expected for this contour (GWM). These figures illustrate the hundreds of structures that will be available to constrain the 3-D genus in the complete SDSS.

In order to quantify the topology of the three-dimensional large-scale structure in our mock redshift catalog, we follow the approach outlined by GMD and GWM. We start with the galaxy density field ( $\delta$ -functions at the location of galaxies) and smooth it with a smoothing function  $W(r) = e^{-r^2/2R_s^2}$ , with  $R_s$  larger than the mean interparticle separation, to produce a smoothed density field. Isodensity contour surfaces can then be constructed, and the genus  $G_{3D}$  of such a surface can be defined as

$$G_{3D} = \text{No. of Holes} - \text{No. of isolated regions}, \quad (4)$$

where “hole” means hole like a donut has and “isolated region” refers to a topologically separate, isolated structure. For example, a surface density contour surface which consisted of 10 spherical pieces each surrounding an isolated spherical cluster would have a genus of  $G_{3D} = -10$ . GMD prove that

$$G_{3D} = -\frac{1}{4\pi} \int K dA, \quad (5)$$

where  $K$  is the Gaussian curvature ( $= 1/r_1 r_2$  where  $r_1$  and  $r_2$  are the two principal radii of curvature) and the integral is performed over the contour surface. Contour surfaces can be labeled by the  $\nu$  value, which is related to the volume fraction of space  $f$  that they enclose:

$$f = \frac{1}{(2\pi)^{1/2}} \int_{\nu}^{\infty} e^{-t^2/2} dt. \quad (6)$$

In the case of a Gaussian one-point probability distribution, the value of  $\nu$  in equation (6) is equal to  $\delta/\sigma$ , the density contrast in units of the standard deviation. The definition of contours in terms of fractional volume rather than density contrast greatly reduces the influence of non-linear gravitational evolution and biased galaxy formation on the genus curve, a point emphasized by GMD and GWM.

For a Gaussian random phase distribution, the genus per unit volume is

$$g_{3D}(\nu) = A(1 - \nu^2) \exp(-\nu^2/2), \quad (7)$$

where

$$A = \frac{1}{(4\pi)^2} \frac{\int P(k) k^2 d^3k}{\int P(k) d^3k} \quad (8)$$

and  $P(k)$  is the power-spectrum of the smoothed density field (Doroshkevich 1970; Adler 1981; Bardeen et al. 1986; Hamilton, Gott & Weinberg 1986). The median density contour which encloses half the volume ( $\nu = 0$ ) is sponge-like ( $g_{3D} > 0$ , i.e., many holes, see Fig. 3(a)). For  $f < 0.16$ ,  $\nu > 1$ , we have  $g < 0$ , showing that we expect to see isolated clusters [see Fig. 3(b)]. Numerous N-body experiments have shown that models which start off with Gaussian random phase initial conditions, as we might expect from an inflationary model (where the fluctuations are due to random quantum noise), retain density fluctuations with an approximately random phase topology into the mildly non-linear regime (e.g., Melott, Weinberg, & Gott 1988). Since the biased galaxy density is generally a monotonic function of the underlying mass density, even the biased galaxy distribution will be approximately random phase when the contours are defined by the volume fraction they enclose. However, important small deviations from random phase topology can occur. Biasing, which systematically locates more proto-galaxies near peaks in the initial density field, produces a small shift in the random phase topology curve (see equation [7]) to the left, a “meatball shift” indicating a slight preference for isolated clusters over isolated voids. Non-linear gravitational evolution can also lead to a meatball shift if the smoothing length  $R_s$  is of order the correlation length. Non-linear gravitational evolution and biasing can interact with each other to produce an enhanced meatball effect in the standard CDM model (Park & Gott 1991b). Because of these effects, the standard biased CDM  $\Omega h = 0.5$ ,  $b = 2$  model produces a slight meatball shift in the genus curve. The hot dark matter model, in which small scale power is damped by Landau damping, shows a slight bubble shift (to the right) in the non-linear regime because voids inflate to larger volume (Melott et al. 1988). Whether non-linear gravitational effects will produce a slight bubble shift or a slight meatball shift in the topology depends on the slope of the power spectrum at approximately the correlation length scale. Non-linear evolution also causes the amplitude of the genus curve to drop below that of the initial density field (Melott et al. 1988; Park & Gott 1991b; Springel et al. 1998).

The points in Figs. 4(a) and 4(b) show genus curves measured from a volume-limited sample of our mock SDSS catalog, in real space and redshift space, for smoothing lengths of  $R_s = 5h^{-1}\text{Mpc}$  and  $R_s = 10h^{-1}\text{Mpc}$  respectively. Fig. 4(a) derives from a sample with a depth of  $R_{max} = 500h^{-1}\text{Mpc}$ , while Fig. 4(b) derives from a sample out to  $R_{max} = 300h^{-1}\text{Mpc}$ , so that in each case the mean separation of galaxies is approximately equal to the smoothing length. We use a procedure similar to that developed by Gott et al. (1989) for measuring the topology of existing galaxy redshift surveys. We first create a galaxy density field on a grid representing a cube  $1000h^{-1}\text{Mpc}$  on a side, then convolve this density field with a Gaussian smoothing filter,

$$S(r) = \frac{1}{2\pi^{3/2} R_s^3} \exp\left(\frac{-r^2}{2R_s^2}\right), \quad (9)$$

using the fast Fourier transform (FFT). We set the smoothing length  $R_s$  equal to the mean separation  $\bar{d}$ . With this definition,  $R_s$  is larger by  $\sqrt{2}$  than the smoothing parameter  $\lambda$  used by

Gott et al. (1989), and this smoothing criterion is therefore more conservative than that used by Gott et al. (1989) and other observational analyses, which have typically set  $\lambda \approx \bar{d}$ . Because of the enormous number of galaxies in the Sloan sample, we can afford to use a smoothing criterion that suppresses shot noise more completely.

We set the galaxy density to zero outside the survey volume, so we must normalize the smoothed density at a given location by the fraction of the smoothing window that lies within the survey. Technically, we achieve this by creating a “mask” array that is one within the survey volume and zero outside, smoothing this mask, and dividing the smoothed galaxy density field by the smoothed mask (see Melott & Dominik 1993). The effective smoothing volume near the survey boundary is thus smaller than the smoothing volume in the bulk of the survey by up to a factor of two. In order to avoid any systematic biases arising in these border cells, we measure the topology only in the volume within which the smoothed mask has a value of at least 0.8, implying that at most 20% of the smoothing window extends outside of the sample.

The dark points in Figs. 4(a) and 4(b) show the results of applying this procedure to the simulation’s real-space galaxy density field. We compute the genus using a slightly modified version of the program CONTOUR (Weinberg 1988), which is based on the curvature summation algorithm proposed by GMD (for an alternative algorithm see Coles, Davies, & Pearson 1996). We use 27 values of the threshold parameter  $\nu$  (as defined by volume fraction  $f$  as described above), ranging from  $\nu = -3.25$  to  $\nu = 3.25$  in steps of 0.25. We reduce small scale jitter in the genus curve by averaging over small ranges in  $\nu$ : a point at  $\nu$  actually represents the average genus of contours at  $\langle g \rangle(\nu) = 0.2 \cdot \sum g(\nu + \{-0.05, -0.025, 0, 0.025, 0.05\})$ .

Ideally, we would estimate errors in the genus curve—and the covariance matrix of the errors—using a large number of mock catalogs like the one analyzed here, each drawn from an independent N-body simulation. By the time the Sloan survey is complete, a computationally ambitious approach like this may be feasible. For the present we rely on a less demanding procedure, using variation within subsets of the sample to estimate the uncertainty in the mean result. We divide the survey volume into four quadrants along the symmetry axes of the survey ellipse. We measure the topology separately in each of these four quadrants and compute a  $1-\sigma$  error bar at each value of  $\nu$  from the  $1-\sigma$  dispersion of the genus in each of the four quadrants divided by  $\sqrt{3}$ . (The distribution of errors is in this case expected to follow a Student’s  $t$ -distribution for  $N = 4$ , cf. Colley [1997]).

The results obtained from the mock catalog agree with the results from the full cube at about the level expected from the  $1-\sigma$  error bars, indicating that our techniques for dealing with the finite survey volume do not introduce systematic biases and that the quadrant procedure yields reasonable error estimates.

The open points in Figs. 4(a) and 4(b) show the genus curve obtained from the redshift space galaxy distribution, with error bars estimated from the dispersion of values in the four quadrants. Peculiar velocities have only a small systematic effect on the genus curve, raising it slightly at

$\nu \gtrsim 1$  and lowering the peak slightly at  $\nu \approx 0$ . Matsubara (1996) noted that in the linear regime, peculiar velocity distortions (Kaiser 1987) cause the genus curve in redshift space to decrease in amplitude relative to the real space genus curve while retaining the same theoretical form.

We observe in Figs. 4(a) and 4(b) that the genus curve shows no discernible left-right shift (the peak is still at  $\nu = 0$ ), but there are slightly more clusters observed at  $\nu = 1$  than voids at  $\nu = -1$ . This effect of non-linear gravitational evolution was first pointed out by Park and Gott (1991b), who noted its presence in the genus curves of evolved CDM mass distributions. They also noted that the effect was more pronounced in the biased particle distributions because of the additional impact of biasing.

Matsubara (1994) has calculated the expected behavior of the genus of Gaussian random phase initial conditions after weakly non-linear gravitational evolution. He provides a perturbative analysis of the genus, in which odd terms in  $\nu$  add to the usual, even  $(1 - \nu^2)$  term in the three-dimensional genus curve for Gaussian random phase fields. Note that Matsubara (1994) uses the definition  $\nu_\sigma = \delta/\sigma$  instead of the implicit definition in terms of volume fraction that we adopt (eq. [6]). The two definitions are identical only when the one-point probability distribution is exactly Gaussian. Matsubara’s relevant result for the three-dimensional genus is the equation

$$G_{3D}(\nu_\sigma) = Ae^{-\nu_\sigma^2/2} \left\{ -H_2(\nu_\sigma) + \sigma \left[ \frac{S}{6}H_5(\nu_\sigma) + \frac{3T}{2}H_3(\nu_\sigma) + 3UH_1(\nu_\sigma) \right] + O(\sigma^2) \right\}, \quad (10)$$

where we have introduced a number of new terms. The  $H_n$ ’s are Hermite polynomials of order  $n$  ( $H_1 = \nu_\sigma$ ,  $H_2 = \nu_\sigma^2 - 1$ ,  $H_3 = \nu_\sigma^3 - 3\nu_\sigma$ ,  $H_5 = \nu_\sigma^5 - 10\nu_\sigma^3 + 15\nu_\sigma$ ), and  $\sigma$  is the r.m.s. fluctuation in the smoothed galaxy distribution.  $S, T$  and  $U$  are tabulated by Matsubara (1994) for various power spectra, the most relevant of which is  $n = -1$ .

In Fig. 5, we have plotted the genus in terms of both our usual  $\nu$  definition for density thresholds, and in terms of strict standard deviations ( $\nu_\sigma$ ), as Matsubara (1994) recommends. Also, we have restricted the range of the plot to reflect the limits suggested by Matsubara & Suto (1996),  $-0.2 \leq \nu\sigma \leq 0.4$ . The heavy solid curve shows the random phase theoretical form,  $g_{3D} = -AH_2(\nu)e^{-\nu^2/2} = A(1 - \nu^2)e^{-\nu^2/2}$ , that best fits the data points obtained from the SSDSS (in real space), with the amplitude  $A$  treated as a free parameter. Springel et al. (1998) suggest using the amplitude drop, the ratio of the fitted value of  $A$  to the value computed from the measured power spectrum via equation (8), as a diagnostic for the degree of non-linear gravitational evolution, and Canavezes et al. (1998) exploit this method to good effect in their analysis of the PSCZ redshift survey. We have not incorporated this technique into our present analysis, but it will certainly be valuable for the analysis of the real SDSS.

For our fits of the pure Gaussian form of the genus curve, the  $\chi^2$  values (calculated assuming a diagonal covariance matrix with 6 degrees of freedom) are 33 for  $\nu$  and 102 for  $\nu_\sigma$ . If we allow ourselves to fit for the odd terms ( $S, T$  and  $U$ ) in  $\nu$ , we obtain the dashed curves, for which the  $\chi^2$  values are reduced to 10 and 7, respectively. These rather dramatic reductions indicate significant improvement in the fits, well beyond that expected by fitting three new independent parameters

alone (in which case  $\chi^2$  should decrease by 3, for three fewer degrees of freedom).

If we do not fit for  $S$ ,  $T$ , and  $U$  but instead use the values implied by Matsubara's (1994) analysis given the value of  $\sigma = 0.408$  measured from the SSDSS density field smoothed at  $10h^{-1}\text{Mpc}$ , then we obtain the dotted line in Fig. 5. This line improves the fit over random-phase for the  $\nu_\sigma$  genus points (open points), but is a worse fit for our usual  $\nu$  points (filled points) than the original random-phase curve (with  $\chi^2$  values of 56 for  $\nu_\sigma$  and 144 for  $\nu$ ). In Table 1, we have tabulated our fit values for  $S$ ,  $T$  and  $U$  and listed the values expected by Matsubara (1994). While it seems that the genus curve is distorted by non-linear evolution in the direction predicted by Matsubara (1994), the amplitude of the distortions in the simulation is significantly smaller. Matsubara & Suto (1996) have also compared cosmological simulations to these predictions and found somewhat better agreement in some cases, particularly when  $\sigma$  is lower than our 0.408 value.

It is perhaps not surprising that Matsubara's perturbative treatment breaks down when the r.m.s. fluctuation amplitude is as large as  $\sigma = 0.408$ . For example, in Matsubara (1994), at large  $\sigma$ 's the genus becomes sponge-like again for  $\nu < -2$ . Since his theoretical genus curve shows isolated voids for  $\nu = -2$ , the only way to obtain a positive genus for  $\nu < -2$  is if these isolated voids begin to look like isolated sponges at lower density thresholds, which seems implausible. By examining Fig. 1, of Matsubara (1994), we have found an approximate relation,  $\nu \gtrsim -1.7 - 0.18/\sigma$ , which describes the plausible applicability of the Matsubara's treatment (for  $n = 1$ ).

The SSDSS redshift catalog yields spectacularly precise measurements of the genus curve at these smoothing lengths ( $5h^{-1}\text{Mpc}$  and  $10h^{-1}\text{Mpc}$ ). These genus curves clearly indicate (as they should) that the initial conditions were random phase (which they were). The departures from the pure Gaussian form of the genus curve, while subtle, are detected at high statistical significance, and they have the form predicted for non-linear evolution by Matsubara (1994) but lower amplitude.

## 5. The Topology of the Peculiar Velocity Field

The biggest uncertainty in mapping the mass density field comes from the fact that the observed luminosity density field does not necessarily follow the true mass density field. This problem, known as “biasing,” prevents us from being able to map the mass density field directly with great confidence.

We can circumvent biasing uncertainties by considering galaxies to be tracers of the peculiar velocity field rather than the density field. If the gravitational instability picture is valid, peculiar velocities uniquely reflect the mass density field. Bertschinger & Dekel (1989) argue that when adopting this approach, any type of galaxy, cluster, or massive object can serve as a test body whose motion is driven by the true density field. Moreover, the peculiar velocity field on a given scale responds to fluctuations of a larger scale in the density field. Since mass density fluctuations on large scales obey linear theory better than fluctuations on small scales, this difference in range

is to our advantage.

We can use the peculiar velocity field in our topological study of large-scale structure. If the density field is Gaussian (random phase), then the potential field is also Gaussian, and in the linear regime, the peculiar velocity field, being the gradient of the Gaussian potential field, should also be Gaussian (see e.g., Bardeen et al. 1986; Park et al. 1992). The *radial* peculiar velocity field (which is the only measurable component of the 3D velocity field), with the value of the peculiar radial velocity treated as a scalar, is also Gaussian in this case (A. J. S. Hamilton, private communication). Thus, we can extract information about large-scale structure by examining the topology of the radial peculiar velocity field. For example, if, by measuring the genus curve of the radial peculiar velocity field (i.e., measuring the genus of iso-velocity surfaces), we find that it is not Gaussian, we must conclude that the density field is also not Gaussian.

The SDSS will provide high resolution spectra for approximately  $10^6$  galaxies. In addition to redshifts, spectra will provide other information, including line-widths and velocity dispersions. These measurements can be used to obtain redshift-independent distance estimates to galaxies using methods such as the Tully-Fisher (TF; Tully & Fisher 1977) relation for spiral galaxies, the Faber-Jackson (FJ; Faber & Jackson 1976) and  $D_n$ - $\sigma$  (Dressler et al. 1987; Lynden-Bell et al. 1988) relations for elliptical galaxies, and the Brightest Cluster Galaxy (BCG; Hoessel 1980; Lauer & Postman 1994) relation. These methods typically yield r.m.s. distance errors of 15% for an individual galaxy. The TF relation can typically be applied to SDSS spiral galaxies only if their redshifts are  $z \gtrsim 0.05$  because at smaller distances the 3"-diameter fiber aperture of the SDSS spectrographs does not subtend enough of the galaxy to yield a correct H $\alpha$  line width. Even with this restriction, we anticipate that the SDSS will obtain redshift-independent distances for nearly 250,000 galaxies (Knapp et al. 1997).

We treat the simulation as a realistic data set by imbuing individual galaxies with 15% distance errors, creating an “observed” catalog that contains true redshifts of all the galaxies (since redshifts can be measured to high precision) and estimates of the galaxies’ distances. We treat this “observed” catalog in the same way we would treat the real SDSS dataset. We give the galaxies estimated radial peculiar velocities

$$V_r = cz - H_0 d, \quad (11)$$

where  $d$  represents the galaxies’ estimated distances (with 15%  $1\sigma$  errors) and  $z$  represents the galaxies’ true redshifts. In order to create the radial peculiar velocity field, we place the galaxies (with their estimated values of  $V_r$ ) at their redshift distances, since at  $z \gtrsim 0.05$  the error due to the 15% scatter in estimated distances greatly exceeds the few hundred km s $^{-1}$  error due to typical galaxy peculiar velocities. It is not to our advantage to go out to the full depth of the survey because the further out we go the larger the errors in the velocity field become. We therefore limit the velocity survey at an outer depth of  $r_{max} = 300h^{-1}$  Mpc.

Once we have radial peculiar velocity estimates for all the galaxies in our survey volume, we smooth the data in order to obtain the smoothed large-scale radial velocity field. The velocity

estimates for individual galaxies have large uncertainties that are generated by the uncertainties in the distance measurements. The peculiar velocities of individual galaxies are usually much smaller than these uncertainties, making them impossible to determine individually. By smoothing, however, we effectively bin the velocity data in smoothing volumes, each containing a large number of individual data points. In this way we can beat down the noise in the  $V_r$  field (velocity errors are divided by  $\sqrt{N}$ , where  $N$  is the effective number of galaxies contained in one smoothing volume). We smooth the simulated data with a Gaussian filter of smoothing radius  $R_s = 21h^{-1}\text{Mpc}$ . With this choice of smoothing length, the expected number of galaxies per smoothing volume at the outer edge of the velocity survey is  $\sim 1100$ , and the expected r.m.s. error in the smoothed radial velocity field is  $\sim 130 \text{ km/s}$ . Of course, the error decreases at smaller distances.

There is one further correction that needs to be made to the “observed” smoothed radial peculiar velocity map. We subtract from it a smoothed correcting map which contains the velocity field  $V'_r = H_0\Delta d$  (i.e.  $V_r = 0$ ), where  $\Delta d$  values are simply different randomly generated 15% (1- $\sigma$ ) distance errors for the galaxies than those previously used. This simple correction gets rid of systematic (Malmquist-type) effects quite well.

As we did for the galaxy density field, we calculate the genus of iso-velocity contours in the smoothed radial velocity field using CONTOUR and estimate errors by breaking the survey volume into four identical (in shape and volume) sub-volumes and computing the scatter in the four independent estimates of the genus.

Fig. 6 shows the True and “Observed” smoothed radial peculiar velocity fields (note that this is a different slice than shown in Fig. 2). From Fig. 6, it is fairly obvious that the radial peculiar velocity field can be mapped out to a large scale, despite the large uncertainties in our distance measurements. The SDSS data should be sufficient for this purpose. Fig. 6 shows that the “Observed” map captures the most prominent features of the True map. There is some distortion, as expected, but overall the maps compare reasonably. The r.m.s. error in our “Observed” map (i.e., the r.m.s. pixel by pixel difference between it and the True map), 121.0 km/s, is smaller than the actual velocity amplitudes seen in our True map (whose r.m.s. value is 148.8 km/s).

The genus curves for both the True and “Observed” (Fig. 7) radial peculiar velocity fields are very noisy, as expected, because of the small number of resolution elements in our survey volume. Nevertheless, both genus curves are roughly Gaussian (the theoretical curve fits our data points as well as we would expect given the 1- $\sigma$  error bars).

## 6. The 2-D Topology of Redshift Slices

Before discussing the 2-D topology of redshift slices, we should explain the somewhat untraditional coordinate system of the SDSS. A galaxy’s position on the sky is defined by a survey latitude  $\eta$  and a survey longitude  $\lambda$ , but the nature of the constant latitude and constant longitude curves is backwards from the usual; the constant latitude curves are great circles that

connect the survey poles (an *east* pole at  $\delta = 0$ ,  $\alpha = 18^h 20^m$  and a *west* pole at  $\delta = 0$ ,  $\alpha = 6^h 20^m$ ), and the constant longitude curves are small circles centered on these poles. The SDSS imaging observations are carried out in scanning mode (see Gunn et al. 1998), and the constant latitude curves are the scan tracks.

Since imaging must precede spectroscopy in any given area of the survey, an early product from the SDSS is likely to be redshift survey slices, much like those of the LCRS. We have therefore selected six slices of constant survey latitude from the mock redshift catalog for 2-D topological analysis. These slices are centered on arcs of constant  $\eta$ , but they have constant angular width in the sky, not constant  $\Delta\eta$ ; thus, while the slices' centers are great circles, their upper and lower boundaries are not. In order to allow more direct comparison to existing results from the LCRS, we have made these slices  $1.5^\circ \times \sim 80^\circ$ , rather than the  $2.5^\circ \times 130^\circ$  of a full SDSS imaging stripe. We choose three slices at low latitude ( $\eta = -33^\circ, -30^\circ, -27^\circ$ ) and three at high latitude ( $\eta = 27^\circ, 30^\circ, 33^\circ$ ), again to obtain a sample similar to that of the full LCRS.

The galaxy sample in the SSDSS is, roughly speaking, magnitude-limited at  $m_{max} = 17.9$  in  $r'$  (see Section 3). As with any magnitude-limited survey, conversion of counts to real galaxy density requires a good understanding of selection effects. We can compensate for these effects by constructing the two-dimensional selection function, which at a given radius reflects the expected surface density of galaxies in the survey.

First we find the maximum distance,  $D_{max,i}$ , at which the  $i$ th galaxy (with actual distance  $D_i$  and magnitude  $m_i$ ) could be seen. To a good approximation, this maximum distance is

$$D_{max,i} = D_i \cdot 10^{0.2(m_{max} - m_i)}, \quad (12)$$

though several small complications exist; we include effects such as limiting surface brightness and  $K$ -corrections in constructing  $D_{max}$ . With each  $D_{max,i}$  computed, we can invoke Schmidt's (1968)  $V/V_{max}$  method to construct the expected volume-density of galaxies as a function of radius,

$$\rho_s(r) = \frac{3}{\Omega_s} \sum_{D_{max,i} > r} D_{max,i}^{-3} \quad (13)$$

(Gott et al. 1989), where  $\Omega_s$  is the solid angle of the slice. We multiply  $\rho_s$  by radius  $r$  to account for the linearly expanding wedge-shaped profile of the slice, and also by a “shape factor”  $S$  (Park et al. 1992) which relates solid angle in the sky to azimuthal angle in the slice map

$$\sigma_s(r) = S r \rho_s(r). \quad (14)$$

Here  $S = [2 \sin(w/2)]$ , where  $w$  is the constant angular width of the slice. Recall that the center of the slice follows a great circle of constant  $\eta$ , which causes a difference from the shape factor given by Park et al. (1992) for declination slices, which do not follow great circles.

We now cut a slice from this azimuthally symmetric selection function with the same longitude spread as the actual slice. We then smooth both the selection function slice and the actual survey

slice with a Gaussian disc,  $e^{-r^2/2R_s^2}$ . When we divide the smoothed survey slice by the smoothed selection slice, we have a map where the effects of the flux limit (and edge effects) have been minimized. We truncate the slice at the radius where the smoothing length,  $R_s$ , equals  $\sigma_s^{-1/2}$  to avoid shot noise sampling effects (we actually truncate one smoothing length inside of that radius to reduce these effects further).

We have chosen our smoothing length to ensure that most of the structures detected are well within the linear regime, because in the linear regime fluctuations at fixed position simply grow in amplitude in proportion to the growth factor, so that the topology of the present-day fluctuations is similar to the topology in the initial fluctuations. Non-linear effects typically become important on scales below about  $8h^{-1}\text{Mpc}$ , so we have chosen a smoothing convolution kernel of  $\exp(-r^2/2R_s^2)$ , with  $R_s = 20h^{-1}\text{Mpc}$ . (As mentioned previously, Matsubara [1996] has shown that peculiar velocities in the linear regime do not distort the form of the genus curve expected for Gaussian fluctuations.)

Fig. 8 provides a contour map of one of the smoothed, calibrated slices ( $\eta = -30^\circ$ , width  $1.5^\circ$ ), with the galaxy locations over-plotted. The heavy lines are contours of high density; the lighter lines are contours of low density, and the dashed line is the median density contour. We will discuss the exact values of these contours below; for now we just wish to illustrate that the contours described correctly identify real over-densities and voids in the data. Also, many “fingers of God” are visible in the data; these are indicators of non-linear effects on small scales (such as virialized clusters). The structures visible in the contours, however, are much larger than the fingers of God, which suggests that we have smoothed out most of the non-linear features in the data (the r.m.s. fluctuation amplitude in the slices is  $\sigma_{20h^{-1}\text{Mpc}} = 0.3$ ).

As with the LCRS, we can immediately note the large number of structures, critical to a quantitative analysis via the genus statistic. When compared with Park et al. (1992), which uses the Geller & Huchra (1989) survey, we find a vast improvement in the number of structures detected (by about a factor of 10), thus a much stronger lever-arm with which to measure topology statistics.

Following Melott et al. (1989) and Gott et al. (1990), we define the two-dimensional genus  $G_{2D}$  of the excursion set for a random density field on a plane as

$$G_{2D} = \frac{(\text{number of isolated high-density regions}) - (\text{number of isolated low-density regions})}{2\pi} \quad (15)$$

Equivalently, the genus can be defined as the total curvature of the contours. Assuming a contour defines a differentiable curve  $C$  on the map, its total curvature is given by the integral

$$K = \int_C \kappa ds \equiv 2\pi G_{2D}, \quad (16)$$

where  $\kappa$  is the local curvature,  $s$  parameterizes the curve, and  $G$  is the genus of the contour. An isolated overdense region will contribute +1 to the total map genus and a void (“hole”) in it will

decrease the genus by 1. In practice, contours may cross the edge of the survey region; in that case the partial curves contribute non-integer rotation indices to the genus.

A two-dimensional random phase Gaussian density field will generate a genus per unit area

$$g = A\nu e^{-\nu^2/2}, \quad (17)$$

where  $A$  is a constant and  $\nu$  is the threshold value, related to the area fraction  $f$  by equation (6). The value of  $A$  depends on an integral of the detailed power spectrum of the fluctuations, but in the case of a perfect power-law spectrum with index  $n > -1$ ,

$$A_{n>-1} = \frac{1}{2 \cdot (2\pi)^{3/2} R_s^2}, \quad (18)$$

where  $R_s$  is the Gaussian smoothing length (Melott et al. 1989; see also Adler 1981; Coles 1988; Park et al. 1990; Gott et al. 1992). We have explicitly used the area fraction in order to be less sensitive to non-linear effects and biasing as discussed in Section 4. Simulations have shown that the genus curve defined in this way more reliably reflects the genus curve of the initial fluctuations, whose nature we wish to test.

In Fig. 8, we have plotted the contour map of the smoothed density distributions in one of the SSDSS slices, with contours at  $\nu = \{-2, -1, 0, 1, 2\}$ . The heavy lines represent  $\nu = \{1, 2\}$ , the light lines  $\nu = \{-2, -1\}$ , and the dashed line  $\nu = 0$ . The map shows many excursions at non-zero values of  $\nu$ , while the median contour ( $\nu = 0$ ) wanders through the map rather randomly, as expected.

In Fig. 9, we have plotted as a function of  $\nu$  the mean genus per unit area (averaged from the estimates in each of the six slices). The best-fit theoretical genus curve expected for a random phase Gaussian distribution, equation (17), is shown as a solid curve, with a best-fit value of  $A = 0.7A_{n>-1}$ . The errorbars are the 68% (solid) and 95% (dotted) confidence limits, estimated from the formal Student’s  $t$ -distribution for  $n = 6$  (six slices) (Lupton 1993). This somewhat less familiar distribution is necessary whenever the error is estimated from the data distribution directly, as opposed to an independent estimation of the error (see Colley 1997). The  $t$ -distribution is equivalent to a Cauchy (Lorentzian) distribution for  $n = 2$ , but it converges to a Gaussian distribution quite rapidly (by  $n = 20$ , the difference from Gaussian is negligible in most applications). The  $t$ -distribution has broad wings to allow for accidentally low sample variances ( $s^2$ ), which cause the  $t$ -variate,  $(\bar{x} - \mu)/(s/\sqrt{n-1})$ , to reach anomalously high values relative to the normal variate,  $(\bar{x} - \mu)/(\sigma/\sqrt{n})$ , ( $\bar{x}$  is the sample mean,  $\mu$  is the true mean, and  $\sigma$  is the true standard deviation).

The Gaussian-field theoretical curve (solid line) in Fig. 9 fits the SSDSS data points reasonably well. To be more quantitative about this, we perform a test related to the  $\chi^2$  statistic. Our “not-quite  $\chi^2$  statistic,”  $\tilde{\chi}^2$ , is computed in the usual way, but is different from a formal  $\chi^2$  in that we have used the formal  $1-\sigma$  errors as estimated from the six slices (recall the genus measurements

are  $t$ -distributed variates, not Gaussian),

$$\tilde{\chi}^2 = \sum_{i=1}^{21} \frac{(\bar{g}_i - \tilde{g}_i)^2}{\sigma_{\bar{g}_i, \text{est}}^2}. \quad (19)$$

Here, the sum runs over the 21 values of  $\nu$  where we have measured the genus (as shown in Fig. 9);  $\bar{g}_i$  is the mean genus among the six slices at each  $\nu$ -value;  $\tilde{g}_i$  is the value of the fitted solid curve, and  $\sigma_{\bar{g}_i, \text{est}}$  is the formal standard error in the mean as estimated from the six slices. For comparison, we ran  $10^4$  simulations of 20  $t$ -variates with  $n = 6$  (one less than 21, due to the one-parameter fit). We then computed  $\tilde{\chi}^2$  for these datasets, and found that our observed value of 36.4 fell at the 70% confidence level (i.e., one would expect the value of  $\tilde{\chi}^2$  to be less than ours 70% of the time, more 30% of the time). Thus, the results were nearly within a  $1\sigma$  statistical agreement with the fitted curve theoretical curve  $g(\nu) \propto \nu e^{-\nu^2/2}$ .

Although the above test accounts for the non-Gaussian error distribution on individual points, it does not account for the covariance of errors from one value of  $\nu$  to another. As one can see from Fig. 9, the difference between the solid curve and the data points is systematic and coherent: the best-fit curve underestimates  $|g(\nu)|$  at  $\nu > 0$  but overestimates  $|g(\nu)|$  at  $\nu < 0$ . In order to assess the significance of this systematic departure from the Gaussian-field prediction, we turn to a more elaborate statistical technique developed by Colley (1997). Alternative approaches to dealing with correlated errors in genus curves are described by Vogeley et al. (1994), Protogeros & Weinberg (1997), and Springel et al. (1998).

Since the genus values at nearby  $\nu$  values might be correlated (they are measuring essentially the same structures), we should look for a point-to-point correlation among the measured genus values. If the correlation is significant, there will be significant off-diagonal terms in the covariance matrix formed from the genus among the various  $\nu$  values. In this case, the commonly used  $\chi^2$  treatment, which assumes a diagonal covariance matrix, must be replaced by a treatment which explicitly employs the full covariance matrix in the  $\chi^2$  computation. This more formal  $\chi^2$  statistic should be an apt figure of merit for the quality of fit of the theoretical genus curve to the genus values derived from a two-dimensional density field.

Since the point-to-point covariance is not known a priori, we are left to produce independent model fields to estimate the covariance. The model fields are pure Gaussian random phase fields, where each Fourier mode has a random phase and amplitude derived from a Gaussian distribution with a mean of zero, and a variance equal to the value of the power spectrum  $P(|\vec{k}|)$  at the  $\vec{k}$  position of the mode in Fourier space. We used the two-dimensional power spectrum for an  $\Omega = 0.4, \Omega_\Lambda = 0.6, h = 0.6$  cosmology (i.e. the same power spectrum as in the simulation) in generating 100 sets of 6 Gaussian random phase slices with identical physical dimensions to the SSDSS slices. We applied exactly the same smoothing and genus topology routines to each model field as we did to the SSDSS slices, giving us a total of 101 independent model genus datasets, 100 of which are guaranteed to derive from Gaussian, random phase fields. For each model dataset,  $m$ , we computed the best fit theoretical curve, and derived its pairwise covariance between the

various values of  $\nu_i$  and  $\nu_j$ . Model  $m$  has covariance

$$C_{ij,m} = (\bar{g}_{i,m} - \tilde{g}_{i,m})(\bar{g}_{j,m} - \tilde{g}_{j,m}). \quad (20)$$

Treating all datasets equivalently, we leave out each one in turn, and compute from the remaining 100 a model covariance matrix as the average of  $C_{ij,m}$  over the remaining  $m$  values, i.e.  $\langle C_m \rangle_{ij} = \sum_{m' \neq m} C_{ij,m'}/100$ . This allows a direct computation of  $\chi_m^2$  in dataset  $m$ , based on a completely independent covariance matrix.

$$\chi_m^2 = \sum_{i,j} (\bar{g}_{i,m} - \tilde{g}_{i,m}) \langle C_m \rangle_{ij}^{-1} (\bar{g}_{j,m} - \tilde{g}_{j,m}). \quad (21)$$

With this improved figure of merit for the fit, we can compare the fit derived from the observed data with that derived from the 100 model datasets. Without further assumption we may evaluate directly the rank of  $\chi^2$  from the real dataset among the 101  $\chi_m^2$  values. We obtain for the SSDSS dataset a rank of 97 out of 101. The probability of obtaining a result that dramatic by chance is 5 out of 101. The simulated slices are therefore just marginally inconsistent with the pure Gaussian random phase fields at the 95% confidence level. Colley (1997), using identical techniques, found that the LCRS agreed better with the simple Gaussian random phase genus curve, ranking 67th out of 101 in its  $\chi^2$  when compared to pure Gaussian random phase curves. The small but significant departure of the SSDSS from the Gaussian random phase curve is presumably due to non-linear effects of structure growth, since the SSDSS was seeded with Gaussian random phase initial conditions. In the following, we discuss non-linear effects on the genus and assess the statistical distinguishability of the LCRS genus and SSDSS genus.

We reconsider Matsubara's (1994) equation for the 3-D genus curve after weakly non-linear evolution of structure, equation (10). In dropping from three to two dimensions, we would expect the Hermite polynomial indices to drop by one, although the coefficients would not necessarily change in a trivial way. The treatment above fits for the coefficient of  $H_1(\nu) = \nu$ , the only term expected in a purely Gaussian random phase field (eq. [17]). This fit is shown by the solid curve in Fig. 9. If we now allow fitting for even terms, ( $H_0 = 1$ ,  $H_2 = \nu^2 - 1$ ,  $H_4 = \nu^4 - 6\nu^2 + 3$ ) we find a much better fit, shown by the dashed curve in Fig. 9. Adding these terms reduces the number of voids by 8% ( $\nu = -1$ ) and increases the number of clusters by 16% ( $\nu = 1$ ) relative to the best fit with equal numbers of clusters and voids. As in the three-dimensional case, the new terms drastically reduce the  $\chi^2$  of the fit, from 36.4 to 13.1 (even a bit below the expected level of 17), much more of a reduction than 3, as expected when adding three new independent adjustable parameters. We also note that the apparent effects of non-linearity work in the same sign in both the three-dimensional and two-dimensional cases, in that there are slightly more clusters than voids in both cases. The coefficients of the even terms are roughly one order of magnitude smaller than the  $H_1$  coefficient, which again suggests that the effects of non-linearity seem to work in the direction suggested by Matsubara (1994), but not as substantially.

For comparison with real observations, we have included an identical plot to Fig. 9 for the LCRS (Fig. 10). Upon inspection, one sees that, as in the SSDSS, the number of clusters in the

LCRS is larger than the number of voids, but the effect is not as large as it is in the SSDSS. Using identical statistical techniques to those above, Colley (1997) showed that the LCRS genus curve was consistent with a Gaussian random phase genus curve within the  $1\sigma$  confidence limit, while here we have shown that the SSDSS was marginally inconsistent at the  $2\sigma$  (95%) level. In fitting for the non-linear terms in the LCRS, we have found that the coefficients of  $H_0$ ,  $H_2$  and  $H_4$  imply a 6% decrease in voids at  $\nu = -1$ , and a 7% increase in clusters at  $\nu = 1$ , relative to the best fit curve with equal numbers. When compared to the 8% decrease in voids and 16% increase in clusters in the SSDSS, we see that the LCRS genus curve is less distinguishable from random phase than is the SSDSS genus curve. Furthermore adding the three new fit parameters to the LCRS genus curve decreased  $\chi^2$  by only 4, (roughly) as expected when adding three new independent parameters. In the case of the SSDSS, adding the three new parameters decreased  $\chi^2$  by 23, indicating that the new parameters were important to the fit.

A more direct comparison of the LCRS and SSDSS reveals that the genus curves derived from these surveys are consistent with each other. Using the  $\tilde{\chi}^2$  method described in the previous section, we have found that the LCRS and SSDSS are consistent well within the  $1\sigma$  consistency criterion. We now use a covariance matrix method similar to that discussed in the previous section (equations [20] and [21]); however instead of using  $(\bar{g}_{i,m} - \tilde{g}_{i,m})$ , the sample mean minus the best-fit value, as the deviate at the  $i$ th  $\nu$  value, we use  $(\bar{g}_{S,i,m} - \bar{g}_{L,i,\ell})$ , the mean genus value in SSDSS data set  $m$  minus the mean genus value in LCRS dataset  $\ell$ , where each dataset includes six slices. As before, we generated 100 fake datasets with six pure Gaussian random phase slices with identical geometry, power-spectrum and smoothing to those of the “real” datasets, for both the SSDSS and LCRS. This means we have 101 independent datasets for both the SSDSS and LCRS. We then use equations (20) and (21), with the above substitutions to compute  $\chi^2_{\ell m}$  for the 10201 possible combinations of datasets:

$$\langle C_{\ell m} \rangle_{ij} = (10200)^{-1} \sum_{\ell', m' \neq \ell, m} (\bar{g}_{S,i,m'} - \bar{g}_{L,i,\ell'}) (\bar{g}_{S,j,m'} - \bar{g}_{L,j,\ell'}), \quad (22)$$

$$\chi^2_{\ell m} = \sum_{i,j=1}^{21} (\bar{g}_{S,i,m} - \bar{g}_{L,i,\ell}) \langle C_{\ell m} \rangle_{ij}^{-1} (\bar{g}_{S,j,m} - \bar{g}_{L,j,\ell}). \quad (23)$$

We find that  $\chi^2$  for the  $\ell = m = 101$  dataset, where the real datasets of both the LCRS and SSDSS are compared, falls at the 46th percentile of all 10201  $\chi^2$  values, an excellent agreement. This consistency between the LCRS and SSDSS is quite remarkable, as is recognizable when comparing Figs. 9 and 10 directly. In fact, the statistical similarity extends to the best-fit the amplitudes of the genus curves:  $A_{LCRS} = 53$  and  $A_{SSDSS} = 56$  (see equation [17]). The expected error in each amplitude (known from the simulated sets) is of order 3. The consistency between these two datasets indicates that the model cosmology within the simulation produces a remarkably similar genus curve to that derived from the observations.

## 7. Availability of the Mock Catalog

We anticipate making further use of this mock redshift catalog in our own preparations for analysis of the SDSS. In the hope that it may be useful to other researchers both inside and outside the SDSS collaboration, we are making the mock catalog available at <http://www.astronomy.ohio-state.edu/~dhw/ssdss.html> (in the event of questions or difficulties, contact David Weinberg). This catalog complements the set of publicly available 2dF and SDSS mock catalogs described by Cole et al. (1998). The present catalog is drawn from a larger volume simulation [ $(600h^{-1}\text{Mpc})^3$  vs.  $(345.6h^{-1}\text{Mpc})^3$ ] and uses more careful modeling of the SDSS selection criteria. The Cole et al. simulations, on the other hand, have higher gravitational force resolution ( $90h^{-1}$  kpc vs.  $1h^{-1}\text{Mpc}$ ) and cover many cosmological models (20 different sets of cosmological parameters and several biasing schemes). Thus, the present mock catalog is probably more suitable for studies that probe large scales or require careful matching of the anticipated SDSS selection function, while the Cole et al. mock catalogs are more useful for studies aimed at testing the ability of statistical diagnostics to distinguish between cosmological models with surveys the size of 2dF or the SDSS. For those wishing to create mock SDSS catalogs from their own large N-body simulations, the code used to assign galaxy properties and apply the SDSS selection criteria is available on request from David Weinberg. It is not trivial to use, but it is extensively commented.

## 8. Conclusions

We have constructed a mock survey to mimic the SDSS redshift survey of a million galaxies in the North Galactic Cap. We have used a large  $N = 54,872,000$  body simulation with  $\Omega_{CDM} = 0.4$ ,  $\Omega_\Lambda = 0.6$ ,  $h = 0.6$ ,  $b = 1.3$ , which has the Gaussian random phase initial conditions expected from an inflationary model, where perturbations arise from quantum fluctuations in the early universe. We measure the 3-D genus curve in this simulation and find that it indeed exhibits the shape predicted theoretically for Gaussian initial conditions. The SDSS will be able to measure the genus curve with unprecedented precision. A sponge-like topology with  $\sim 500$  holes is measured here, giving a point-wise statistical precision of 4%, a vast improvement over previous surveys. Indeed, the data trace the random phase curve so well that observers confronted with such data would almost certainly conclude (correctly) that the mock universe had started with Gaussian random phase initial conditions. Small deviations from the random phase curve are, however, detectable at high statistical significance, the main effect being a slight excess of clusters over voids that results from non-linear gravitational evolution and biasing (Park & Gott 1991b). Although the influence of non-Gaussianity of primordial fluctuations on the genus curve depends on the specifics of the theoretical model, the numerical studies of the topology of the texture model by Gooding et al. (1992) and of “generic” non-Gaussian models by Weinberg & Cole (1992) suggest that typical non-Gaussian models produce distortions of the genus curve that could be detected easily at the high level of precision obtainable with the SDSSS.

In comparing to predicted effects of non-linear structure growth on the genus (Matsubara 1994), we find the measured effects to be consistent in sign but not in magnitude. The Matsubara (1994) formula predicts a much larger (roughly two orders of magnitude) distortion of the genus curve than we observe. This discrepancy may result from using the formula outside its applicable range.

We have also shown how the genus curve of the velocity field may be measured in the SDSS. Again, the results are consistent with the Gaussian random phase prediction, but the statistical precision is very low because a very large smoothing length is required to beat down the noise in redshift-independent distance measurements.

Since the earliest products from the Sloan redshift survey will be 2-D slices, we have measured the topology (genus) of large-scale structure in such slices drawn from the mock survey. Again, we find that the number of clusters slightly exceeds the number of voids, but at a lesser level than would be presumably expected from Matsubara (1994).

Finally, we compare our simulation slices directly with a very similar study of the (observed) Las Campanas Redshift Survey slices (Colley 1997). While both the LCRS and our simulation slices show a slight excess of clusters over voids, the effect is about twice as large in the simulation. The genus of the LCRS slices nonetheless agrees with the genus of the simulation slices, well within the  $1-\sigma$  interval, without any adjustment of amplitude in the curves.

A better understanding of the non-linear structure growth and its effects on the genus curve will come with ever more elaborate cosmological simulations, and with the Sloan Digital Sky Survey itself. A survey this large is a powerful tool for evaluating theories of cosmic structure formation.

This paper is supported by NSF grant AST95-29120 and NASA grant NAG5-2759. We thank Bharat Ratra, Andrew Hamilton, Martin Bucher and Neta Bahcall for helpful conversations. We thank Michael Strauss for computing the K-corrections and galaxy colors used in the mock catalog. DW thanks Jim Gunn, Hans-Walter Rix, and Michael Strauss for numerous helpful discussions on the assignment of galaxy properties, and he acknowledges the support of a Keck fellowship at the Institute for Advanced Study during the early phases of this work. CP acknowledges the support of the Basic Science Research Institute Program, Ministry of Education 1995 (BSRI-98-5408).

## REFERENCES

- Adler, R.J. 1981, *The Geometry of Random Fields*, Wiley, New York
- Bahcall, N. A., Fan, X., & Cen, R. 1998, *ApJ*, 485, L53
- Bahcall, N., & Soneira, R.M. 1983, *ApJ*, 270, 20
- Bardeen, J.M., Bond, J.R., Kaiser, N., & Szalay, A.S. 1986, *ApJ*, 304, 15

Bardeen, J.M., Steinhardt, P.J., & Turner, M.S. 1983, Phys. Rev. D., 28, 679

Bertschinger, E., et al. 1990, ApJ, 364, 370

Blanchard, A., & Bartlett, J. G. 1998, A&A, 332, L49

Broadhurst, T.J., Ellis, R.S., Koo, D.S., & Szalay, A.S. 1990, Nature, 343, 726

Bucher, M., Goldhaber, A.S. & Turok, N. 1995a, Phys. Rev. D., 52, 3314

Bucher, M., Goldhaber, A. S. & Turok, N. 1995b, Phys. Rev. D., 52, 5538

Canavezes, A., Springel, V., et al. 1998, MNRAS, 297, 777

Carlberg, R. G., Yee, H. K. C., Ellingson, E., Abraham, R., Gravel, P., Morris, S., & Pritchett, C. J. 1996, ApJ, 462, 32

Carlberg, R. G., Yee, H. K. C., & Ellingson, E. 1997, ApJ, 478, 462

Cen, R., & Ostriker, J. P. 1992, ApJ, 399, L113

Chiba, M., & Yoshii, Y. 1999, ApJ, 510, 42

Cole, S., Hatton, S., Weinberg, D. H., & Frenk, C. S. 1998, MNRAS, 300, 945

Cole, S., Weinberg, D. H., Frenk, C. S., & Ratra, B. 1997, MNRAS, 289, 37

Coleman, G. D., Wu, C.-C., & Weedman, D. W. 1980, ApJS, 43, 393

Coles, P. 1988, MNRAS, 234, 509

Coles, P., Davies, A. G., & Pearson, R. C. 1996, MNRAS, 281, 1375

Coles, P., Moscardini, L., Plionis, M., Lucchin, F., Matarrese, S., & Messina, A. 1993, MNRAS, 260, 572

Colless, M. 1998, in Wide Field Surveys in Cosmology, 14th IAP Meeting, (Editions Frontieres: Paris), p. 77

Colley, W. N. 1997, ApJ, 489, 471

Colley, W. N., Gott, J. R., & Park, C. 1996, MNRAS, 281, L82

de Lapparent, V., Geller, M., & Huchra, J. 1986, ApJ, 302, L1

de Vaucouleurs, G. 1948, Ann d’Astrophys, 11, 247

Dekel, A., Bertschinger, E., & Faber, S. M. 1990, ApJ, 364, 349

Djorgovski, S., & Davis, M. 1987, ApJ, 313, 59

Doroshkevich, A. G. 1970, Astrophysika, 6, 320

Dressler, A., et al 1987, ApJ, 313, 42

Eke, V. R., Cole, S., Frenk, C. S., & Henry, J. P. 1998, MNRAS, 298, 1145

Evrard, A. E. 1997, MNRAS, 292, 289

Faber, S. M., & Jackson, R. E. 1976, ApJ, 204, 668

Freeman, K. C. 1970, *ApJ*, 160, 811

Fukugita, M., Futamase, T., Kasai, M., & Turner, E. L. 1992, *ApJ*, 393, 3

Fukugita, M., Ichikawa, T., Gunn, J. E., Doi, M., Shimasaku, K., & Schneider, D. P. 1996, *AJ*, 111, 1748

Geller, M. J. & Huchra, J. P. 1989, *Science*, 246, 897

Gooding, A. K., Park, C., Spergel, D. N., Turok, N., & Gott, J.R., 1992, *ApJ*, 393, 42

Gott, J. R. 1982, *Nature*, 295, 304

Gott, J. R. 1986, *Inner Space/Outer Space, The Interface Between Cosmology & Particle Physics*, eds. E. W. Kolb et al. (Chicago: Univ. of Chicago Press), 362

Gott, J. R., et al. 1989, *ApJ*, 340, 625

Gott, J. R., Gao, B., & Park, C. 1991, *ApJ*, 383, 90

Gott, J. R., Mao, S., Park, C., Lahav, O. 1992, *ApJ*, 385, 26

Gott, J. R., Melott, A. L., & Dickinson, M. 1986, *ApJ*, 306, 341 (GMD)

Gott, J. R., Park, C., Juskiewicz, R., Bies, W. E., Bennett, D. P., Bouchet, F. R., & Stebbins, A. 1990, *ApJ*, 352, 1

Gott, J. R., Park, M., & Lee, H. M. 1989, *ApJ*, 338, 1

Gott, J. R., Rhoads, J. E., & Postman, M. 1994, *ApJ*, 421, 1

Gott, J. R. & Statler, T. S. 1984, *Physics Letters*, 136B, 157

Gott, J. R., Weinberg, D. H. & Melott, A. L. 1987, *ApJ*, 321, 2 (GWM)

Gunn, J. E., et al. 1998, *AJ*, 116, 3040

Gunn, J. E., & Knapp, G. R. 1993, in *Sky Surveys: Protostars to Protogalaxies*, ASP Conference Series vol. 43, ed. B. T. Soifer, (ASP: San Francisco), p. 267

Gunn, J. E. & Weinberg, D. H. 1995, in *Wide Field Spectroscopy and the Distant Universe*, eds. S. Maddox & A. Aragón-Salamanca, (Singapore: World Scientific), 3, astro-ph/9412080

Guth, A. H. 1981, *Phys. Rev. D*, 23, 347

Hamilton, A. J. S., Gott, J. R., & Weinberg, D. W. 1986, *ApJ*, 309, 1

Harrison, E. R. 1970, *Phys. Rev. D*, 1, 2726

Hawking, S., & Turok, N. 1998, hep-th/9802030

Hoessel, J. G. 1980, *ApJ*, 241, 493

Kaiser, N. 1987, *MNRAS*, 227, 1

Katz, N., Hernquist, L., & Weinberg, D. H. 1992, *ApJ*, 399, L109

Kauffmann, G., Nusser, A., & Steinmetz, M. 1997, *MNRAS*, 286, 795

Kent, S. M. 1985, *ApJS*, 59, 115

Klypin, A. A., & Kopylov, A. I. 1983, Sov Ast Lett, 9, 41

Knapp, G. R., et al. 1997, proposal to NASA by the SDSS collaboration, available at <http://www.astro.princeton.edu/BBOOK/>

Kogut, A., Banday, A. J., Bennett, C. L., Gorski, K. M., Hinshaw, G., Smoot, G. F., & Wright, E. L. 1996, ApJ, 464, L29

Lauer, T. R., & Postman, M. 1994, ApJ, 425, 418

Lin, H., Kirshner, R. P., Shectman, S., Landy, S. D., Oemler, A., Tucker, D. L., & Schechter, P. 1996, ApJ, 471, 617

Linde, A. D. 1990, Inflation and Quantum Cosmology (Academic Press, Boston)

Linde, A. D. 1995, Phys. Lett. B., 351, 99

Linde, A., & Mezhlumian, A. 1995, Phys. Rev. D., 52, 6789

Lineweaver, C. H. 1998, ApJ, 505, L69

Lupton, R. H. 1993. Statistics in Theory and Practice Princeton University Press, Princeton, NJ, pages 27ff

Lynden-Bell, D., et al. 1988, ApJ, 326, 618

Maddox, S. J., Efstathiou, G., Sutherland, W. J., & Loveday, J. 1990, MNRAS, 242, 43P

Maoz, D. & Rix, H. 1993, ApJ, 416, 425

Margon, B. 1999, Phil Trans Roy Soc Lond A, 357, in press, astro-ph/9805314

Matsubara, T. 1994, ApJ, 434, 43

Matsubara, T. 1996, ApJ, 457, 13

Matsubara, T. & Suto, Y., 1996, ApJ, 460, 51

Melott, A. L., Cohen, A. P., Hamilton, A. J. S., Gott, J. R. & Weinberg, D. H. 1989, ApJ, 345, 618

Melott, A. L., & Dominik, K. G. 1993, ApJS, 86, 1

Melott, A. L., Weinberg, D. H., & Gott, J. R. 1988, ApJ, 328, 50

Moore, B., Frenk, C. S., Weinberg, D. H., Saunders, W., Lawrence, A., Ellis, R. S., Kaiser, N., Efstathiou, G., & Rowan-Robinson, M., 1992, MNRAS, 256, 477

Narayanan, V. K., Berlind, A. A., & Weinberg, D. H. 1998, ApJ, submitted, astro-ph/9812002

Oke, J. B., & Gunn, J. E. 1983, ApJ, 266, 713

Ostriker, J. P., & Steinhardt, P. J. 1995, Nature, 377, 600

Park, C. 1990, PhD Thesis, Princeton University

Park, C. 1990, MNRAS, 242, 59P

Park, C. 1991, MNRAS, 251 167

Park C., Colley, W. N., Gott, J. R., Ratra, B., Spergel, D. N., & Sugiyama, N. 1998, ApJ, 506, 473

Park, C., & Gott, J. R. 1991a, MNRAS, 249, 288

Park, C., & Gott, J. R. 1991b, ApJ, 378, 457

Park, C., Gott, J. R., & da Costa, L. N. 1992, ApJ, 392, L51

Park, C., Gott, J. R., Melott, A., & Karachentsev, I. D. 1992, ApJ, 387, 1

Peacock, J. A., & Dodds, S. J. 1994, MNRAS, 267, 1020

Peebles, P. J. E. 1993, Principles of Physical Cosmology, (Princeton: Princeton University Press)

Peebles, P. J. E., & Ratra, B, ApJ325, L17

Peebles, P. J. E., & Yu, J. T. 1970, ApJ, 162, 815

Perlmutter, S., et al. 1999, ApJ, in press, astro-ph/9812133

Petrosian, V. 1976, ApJ, 209, L1

Plionis, M., Valdarnini, R., & Coles, P. 1992, MNRAS, 258, 114

Protogeros, Z. A. M., & Weinberg, D. H. 1997, ApJ, 489, 457

Ratra, B., & Peebles, P. J. E. 1994, ApJ, 432, L5

Ratra, B., & Peebles, P. J. E. 1995, Phys. Rev. D52, 1837

Ratra, B., & Peebles, P. J. E. 1998, Phys. Rev. D37, 3406

Reichart, D. E., Nichol, R. C., Castander, F. J., Burke, D. J., Romer, A. K., Holden, B. P., Collins, C. A., & Ulmer, M. P. 1998, ApJ, submitted, astro-ph/9802153

Riess, A. G., et al. 1998, AJ, 116, 1009

Roos, M., & Harun-or-Rashid, S. M. 1999, A&A, submitted, astro-ph/9901234

Ryden, B. S. 1992, ApJ, 396, 445

Saunders, W. et al. 1991, Nature, 349, 32

Schechter, P. 1976, ApJ, 203, 297

Schmidt, M. 1968, ApJ, 151, 393

Shandarin, S. F., & Zel'dovich, Y. B. 1989, Rev Mod Phys, 61, 185

Shane, C. D., & Wirtanen, C. A. 1967, Pub Lick Obs, 22, part 1

Shectman, S. A., Landy, S. D., Oemler, A., Tucker, D. L., Lin, H., Kirshner, R. P., & Schechter, P. L. 1996, ApJ, 470, 172

Smoot, G. F. et al. 1994, ApJ437, 1

Smoot, G. F. et al. 1992, ApJ, 396, L1

Springel, V., et al. 1998, MNRAS, 298, 1169

Tegmark, M. 1998, ApJ, submitted, astro-ph/9809201

Tully, R. B., & Fisher, J. R. 1977, A&A, 54, 661

Turner, M. S. 1998, in Critical Dialogues in Cosmology, ed. Turok, N. (Singapore: World Scientific), 555

Viana, P. T. P., & Liddle, A. R. 1998, MNRAS, in press, astro-ph/9803244

Vogeley, M. S., Park, C., Geller, M. J., Huchra, J. P., Gott, J. R. 1994, ApJ, 420, 525

Weinberg, D. H. 1988, PASP, 100, 1373

Weinberg, D. H., & Cole, S., 1992, MNRAS, 259, 652

Weinberg, D. H., Croft, R. A. C., Hernquist, L., Katz, N., & Pettini, M. 1998, ApJ, submitted, astro-ph/9810011

Weinberg, D. H., & Gunn, J. E. 1990a, ApJ, 352, L25

Weinberg, D. H., & Gunn, J. E. 1990b, MNRAS, 247, 260

White, S. D. M., Frenk, C. S., Davis, M., & Efstathiou, G. 1987, ApJ, 313, 505

Wright, E. L. et al. 1992, ApJ, 396, L13

Yamamoto, K., Sasaki, M., & Tanaka, T. 1995, ApJ, 455, 412

Zel'dovich, Ya. B. 1970, A&A, 5, 84

Zeldovich, Ya. B. 1972, MNRAS, 160, 1P

**Table 1**

	predicted	best-fit ( $\nu$ )	best-fit ( $\nu_\sigma$ )
S	3.468	−0.136	0.0501
T	2.312	−0.0314	−0.116
U	1.227	0.129	0.0512

Table 1: Best-fit values of  $S$ ,  $T$  and  $U$  vs. values predicted by Matsubara (1994). In describing the genus of the large-scale distribution of galaxies,  $S$ ,  $T$  and  $U$ , defined in equation (10), are coefficients of odd polynomials which add to the usual 2nd-order even polynomial, expected in the Gaussian random phase genus curve of three dimensions. The second column is for density thresholds described by  $\nu$  (equation 6); the third column is for density thresholds defined strictly by standard deviations  $\nu_\sigma = \delta/\sigma$ . Note that the range of the density thresholds for the fits has been limited to the range suggested by Matsubara & Suto (1996), who give  $−0.2 \leq \nu\sigma \leq 0.4$ , where  $\sigma$  is the standard deviation in density fluctuation at this smoothing length ( $R_s = 10h^{-1}\text{Mpc}$ ,  $\sigma = 0.408$ ).

Fig. 1.— A projection onto the sky of the nearly 1 million galaxies in the Simulated Sloan Digital Sky Survey. The tickmarks indicate the boundaries of the six degree slice in Fig. 2.

Fig. 2.— A six degree slice of the Simulated Sloan Digital Sky Survey

Fig. 3.— (a) Median density contour in the Simulated Sloan Digital Sky Survey, showing its sponge-like form. The observer is at the apex (left) and the radius of the sample is  $500h^{-1}\text{Mpc}$ , and the smoothing length (c.f. equation [9]) is  $R_s = 10h^{-1}\text{Mpc}$ .

Fig. 3.— (b) 93rd density percentile contour in the Simulated Sloan Digital Sky Survey, showing isolated clusters, for the same sample and smoothing length shown in Figure 3(a).

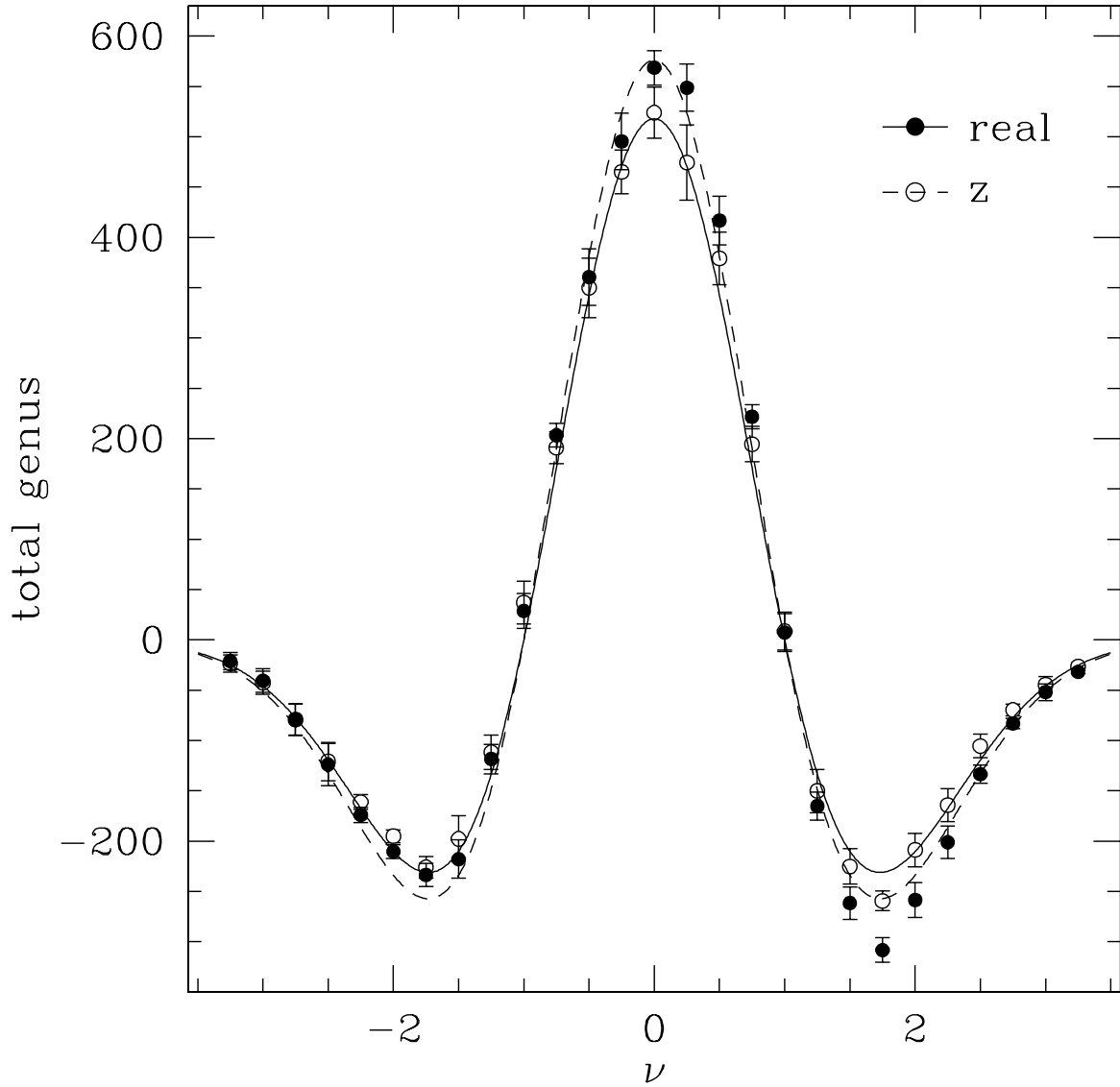


Fig. 4.— (a) The genus curve of three-dimensional structure in the SSDSS, in real space (filled points, and solid curve), and redshift space (open points and dashed curve). The smoothing length is  $R_s = 5h^{-1}\text{Mpc}$ . The curves are the best fit for  $g = A \cdot (1 - \nu^2) \exp(-\nu^2/2)$ , expected for a Gaussian random phase field. Errorbars are  $1-\sigma$  confidence intervals.

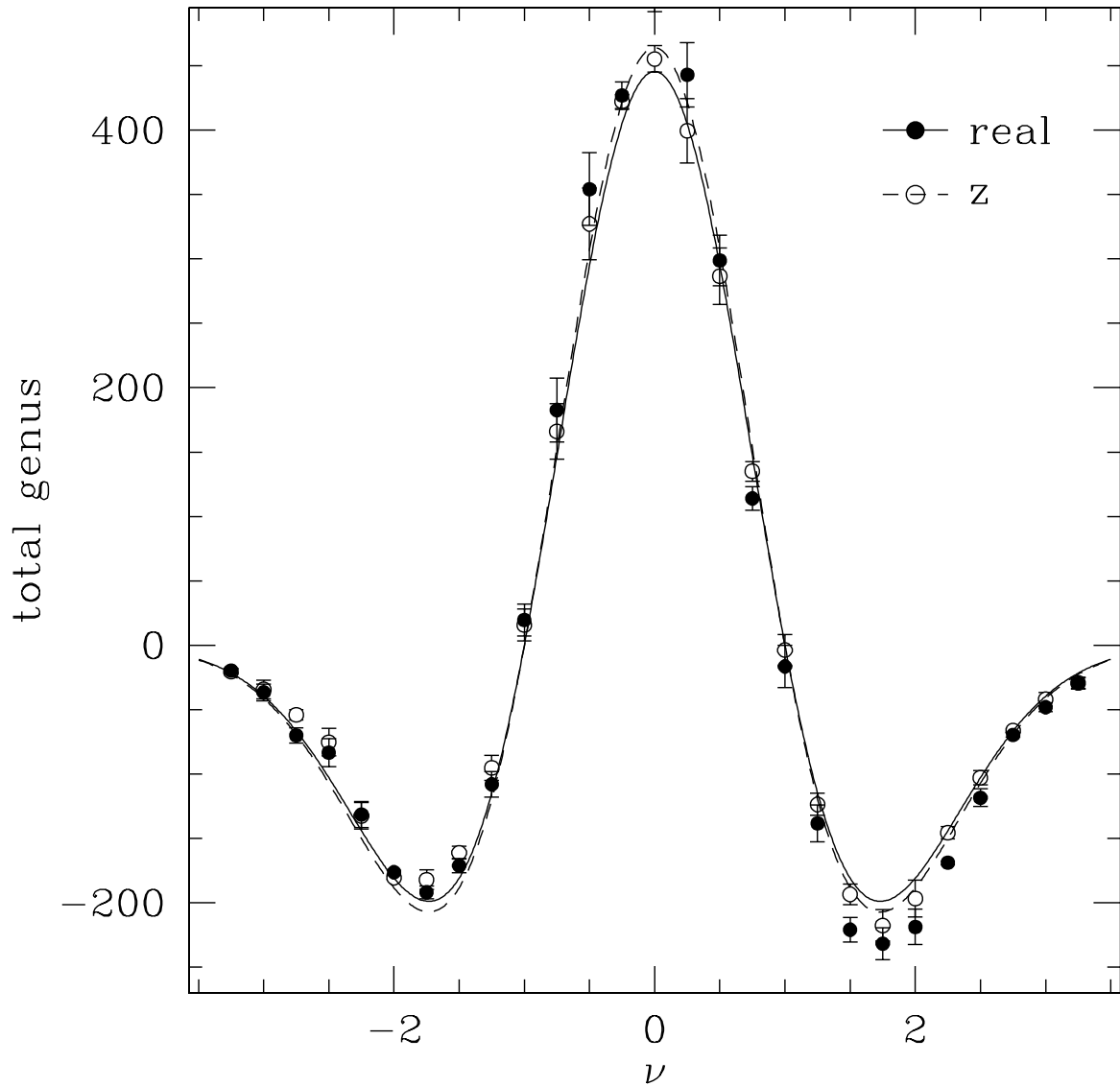


Fig. 4.— (b) as in 4(a), but for a smoothing length of  $R_s = 10h^{-1}\text{Mpc}$ .

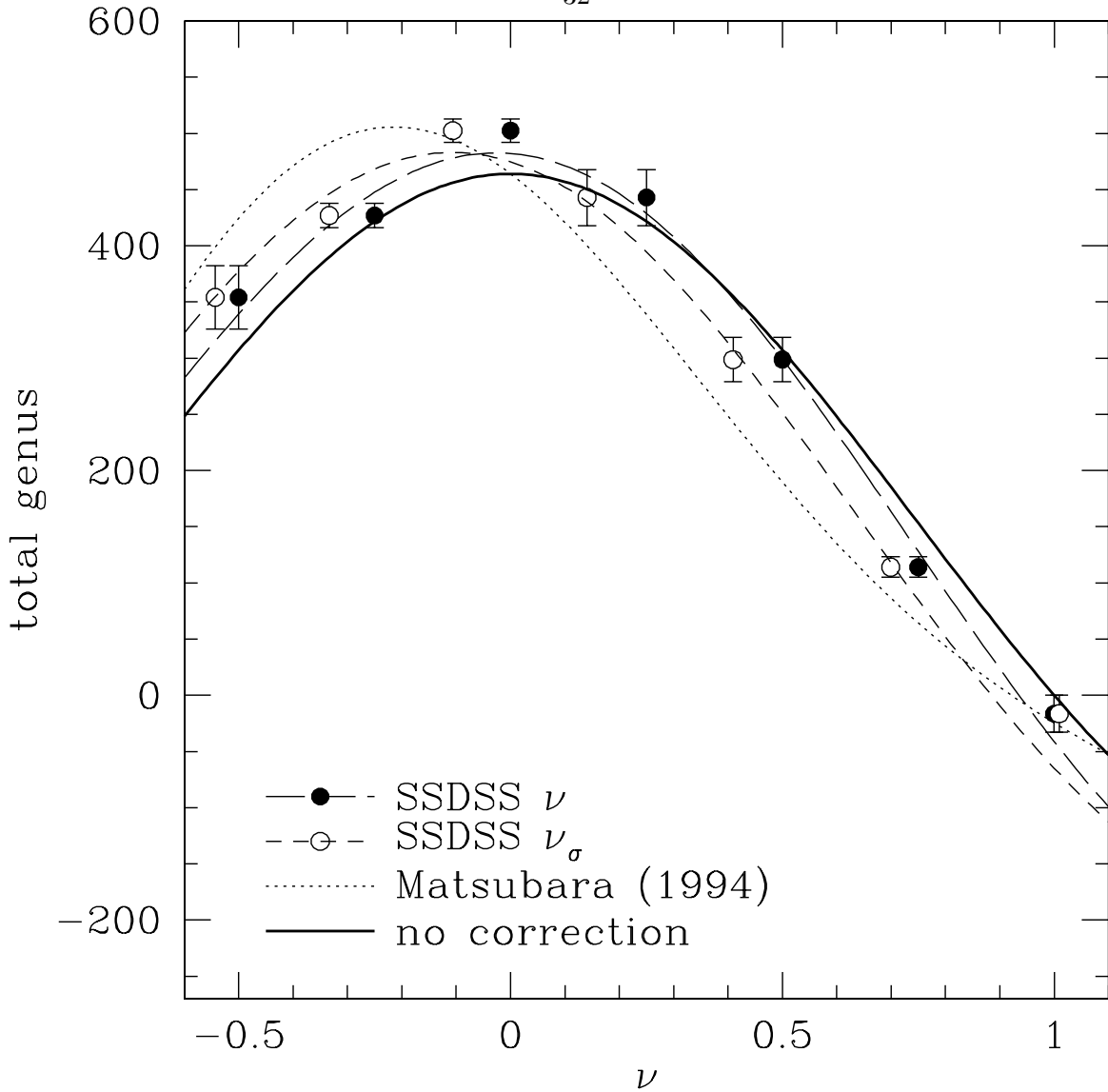


Fig. 5.— Comparison of the 3-D genus with predictions from Matsubara (1994) for weakly non-linear evolution of the genus. The heavy solid curve is the best fit for the purely Gaussian random phase curve. The solid points reflect density thresholds  $\nu$  defined in equation 6; the open points reflect density thresholds which are strict standard deviations  $\nu_\sigma = \delta/\sigma$ . The long- and short-dashed curves include the best fits for amplitude and for  $S$ ,  $T$  and  $U$ , given in equation (10), in terms of  $\nu$  and  $\nu_\sigma$  respectively. These are coefficients of odd terms added to the usual even genus curve. The dotted curve is the prediction of Matsubara (1994). Note that the range of the density thresholds is delimited by Matsubara & Suto (1996), who suggest  $-0.2 \leq \nu\sigma \leq 0.4$ , where  $\sigma$  is the standard deviation in density fluctuation at this smoothing length ( $R_s = 10h^{-1}\text{Mpc}$ ;  $\sigma = 0.408$ ).

Fig. 6.— At top is the true radial peculiar velocity field in a slice of the simulated SDSS. At bottom is the “observed” radial peculiar velocity field. Both fields have been smoothed with a Gaussian filter of radius  $R_s = 21h^{-1}\text{Mpc}$ . The shaded regions have a positive radial peculiar velocity and the shaded contours represent velocities of +50 km/s and +100 km/s. The unshaded regions have a negative radial peculiar velocity and the unshaded contours represent velocities of –50 km/s and –100 km/s.

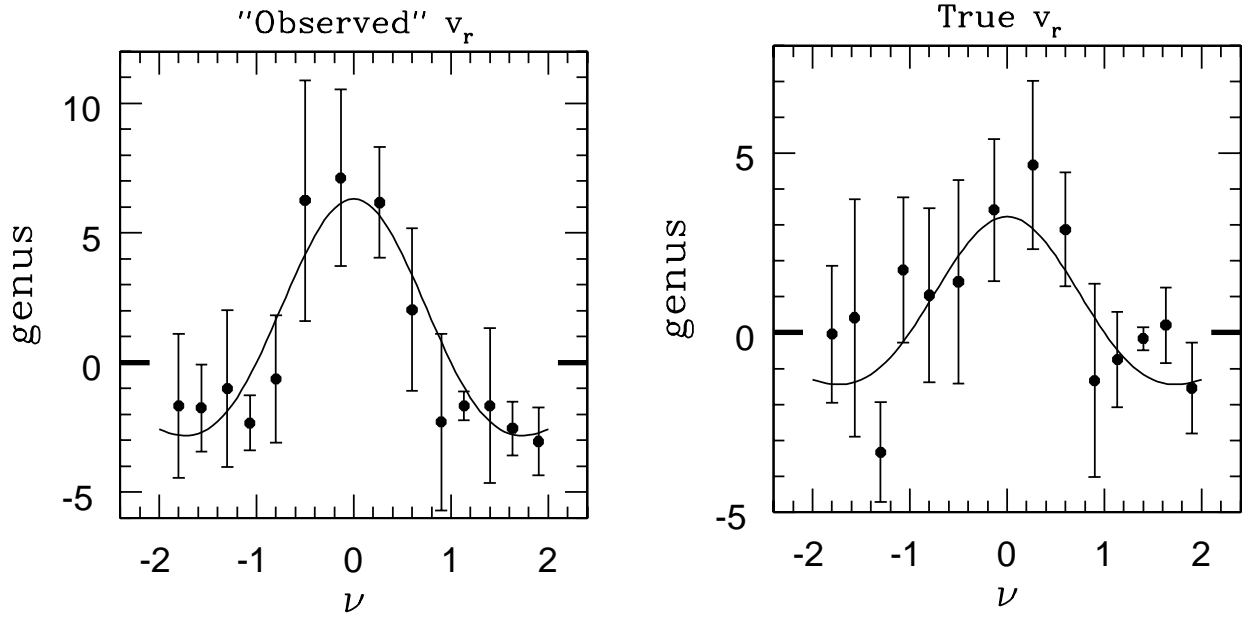


Fig. 7.— The genus curve of the “observed” radial peculiar velocity field (left) and the true radial peculiar velocity field (right) of the SSDSS. Points show simulation measurements with  $1-\sigma$  error bars computed from the variance among four subsets of the survey, and smooth curves show the form expected for a Gaussian field (eq. [7]).

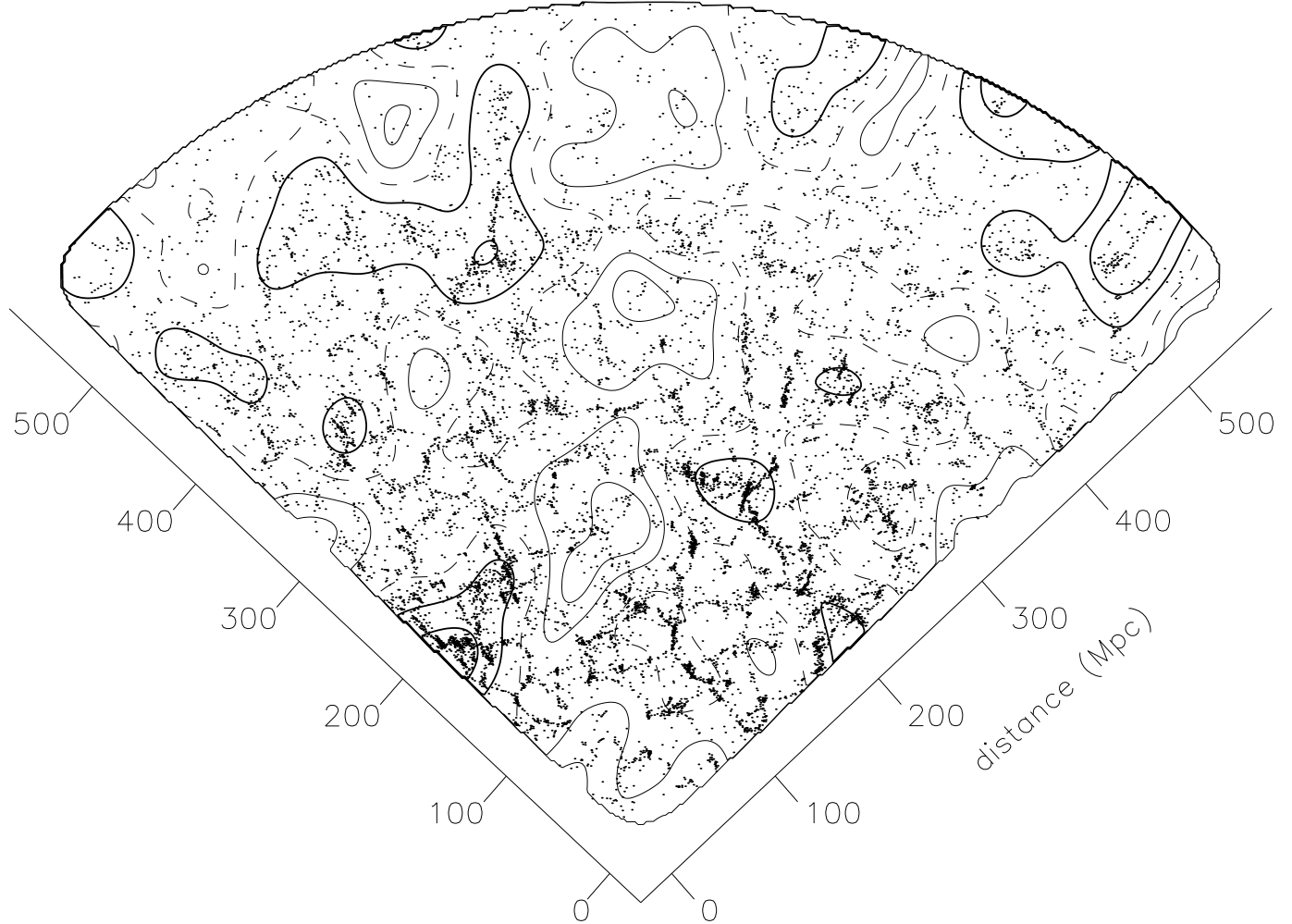


Fig. 8.— Contours of  $\nu = \{-2, -1, 0, 1, 2\}$  in the  $\eta = -30^\circ$  slice of the SSDSS, after smoothing with a Gaussian filter  $e^{-r^2/2R_s^2}$ , with  $R_s = 20h^{-1}\text{Mpc}$ . The median density contour ( $\nu = 0$ ) is dashed. High density contours are heavy and solid ( $\nu = \{1, 2\}$ ); low density contours are light and solid ( $\nu = \{-2, -1\}$ ). Over-plotted are the galaxy locations themselves, so that the location of overdense regions and voids is obvious.

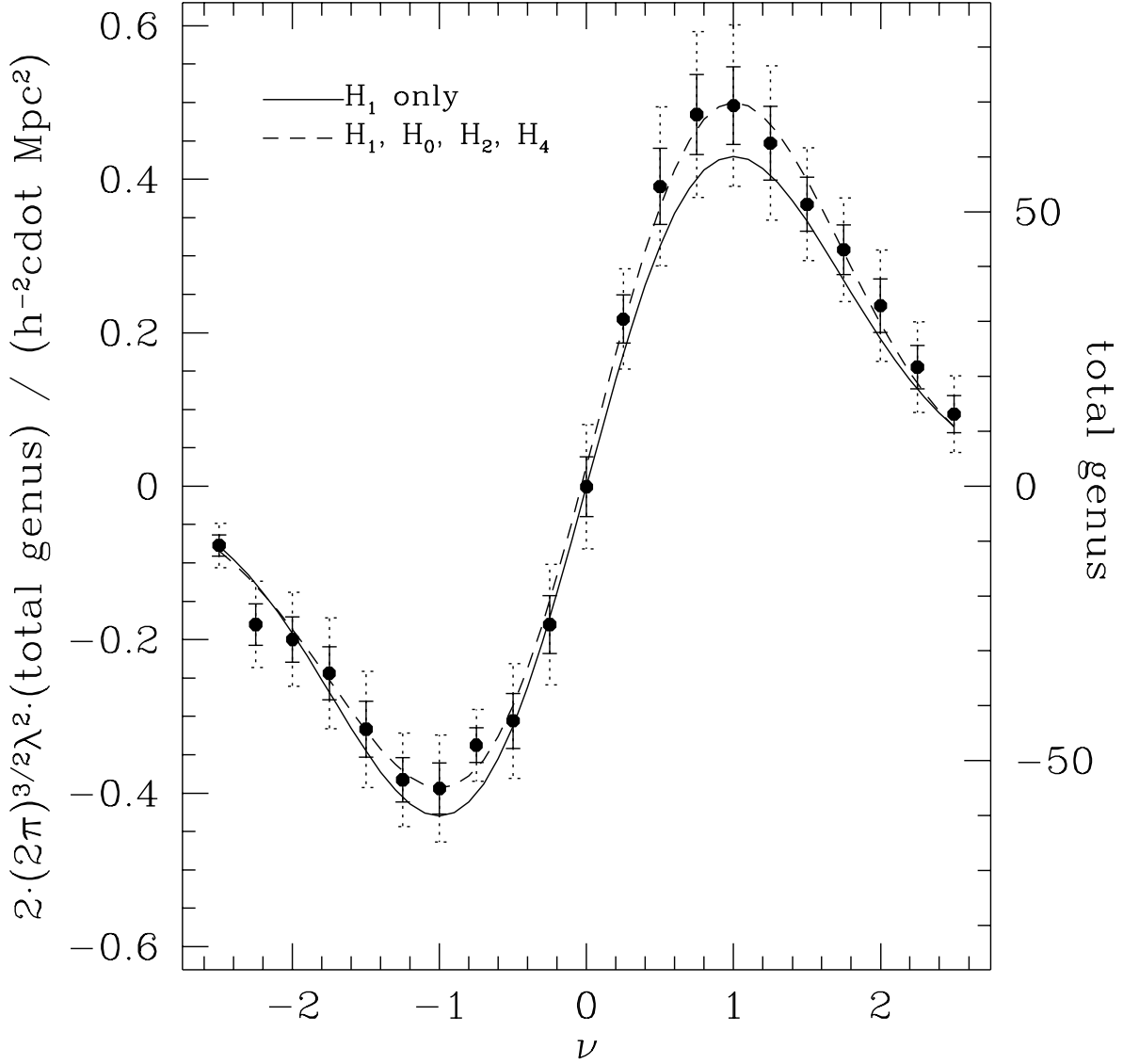


Fig. 9.— The genus curve of two-dimensional structure in SSDSS slices. The smoothing length is  $R_s = 20h^{-1}\text{Mpc}$ . The solid curve is the best fit for  $g = A \cdot \nu \exp(-\nu^2/2)$ , expected for a Gaussian random phase field. The dashed curve is the best fit for  $g = A[H_1(\nu) + BH_0(\nu) + CH_2(\nu) + DH_4(\nu)] \exp(-\nu^2/2)$ , where  $H_n$  is the Hermite polynomial of degree  $H_n$  [ $H_1(\nu) = \nu$ ]. Points are the average results from six  $1.5^\circ$  slices; solid and dotted error bars show the 68.3% and 95% confidence intervals on each  $g(\nu)$  measurement computed using the Student's  $t$ -distribution and the variance among the six slices. The  $y$ -axis is also labeled (on the right) by the total genus in the sample.

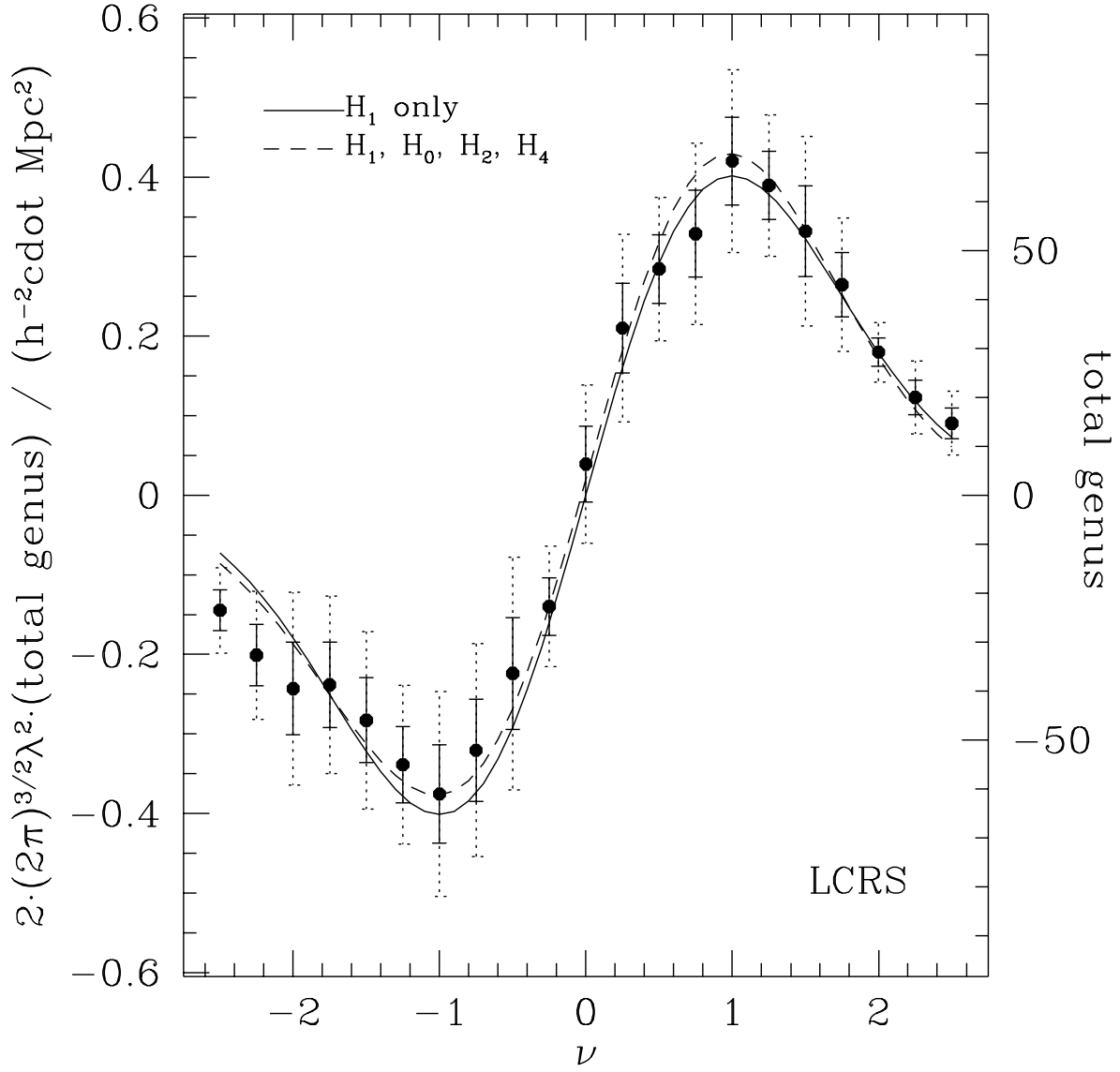


Fig. 10.— As in Fig. 9, but for the Las Campanas Redshift Survey. Notice that the fit is not much improved after adding even terms, as expected when non-linear structure growth is important. In the Simulated SDSS, however, the fit improved substantially.

This figure "colley\_fig1.gif" is available in "gif" format from:

<http://arxiv.org/ps/astro-ph/9902332v2>

This figure "colley\_fig2.gif" is available in "gif" format from:

<http://arxiv.org/ps/astro-ph/9902332v2>

This figure "colley\_fig3a.gif" is available in "gif" format from:

<http://arxiv.org/ps/astro-ph/9902332v2>

This figure "colley\_fig3b.gif" is available in "gif" format from:

<http://arxiv.org/ps/astro-ph/9902332v2>

This figure "colley\_fig6.gif" is available in "gif" format from:

<http://arxiv.org/ps/astro-ph/9902332v2>